nature biotechnology

ARTICLES

https://doi.org/10.1038/s41587-019-0246-4

In vivo CRISPR screening in CD8 T cells with AAV–*Sleeping Beauty* hybrid vectors identifies membrane targets for improving immunotherapy for glioblastoma

Lupeng Ye[1,2,3,12], Jonathan J. Park[1,2,3,4,12], Matthew B. Dong[1,2,3,4,5,6,12], Quanjun Yang[1,2,3], Ryan D. Chow[1,2,3,4], Lei Peng[1,2,3], Yaying Du[1,2,3], Jianjian Guo[1,2,3], Xiaoyun Dai[1,2,3], Guangchuan Wang[1,2,3], Youssef Errami[1,2,3] and Sidi Chen[1,2,3,4,5,7,8,9,10,11]*

Targeting membrane proteins could improve the efficacy of T cell–based immunotherapies. To facilitate the identification of T cell targets, we developed a hybrid genetic screening system where the *Sleeping Beauty* (*SB*) transposon and single guide RNA cassette are nested in an adeno-associated virus (AAV). SB-mediated genomic integration of the single guide RNA cassette enables efficient gene editing in primary murine T cells as well as a screen readout. We performed in vivo AAV–SB-CRISPR screens for membrane protein targets in CD8$^+$ T cells in mouse models of glioblastoma (GBM). We validated screen hits by demonstrating that adoptive transfer of CD8$^+$ T cells with *Pdia3*, *Mgat5*, *Emp1* or *Lag3* gene editing enhances the survival of GBM-bearing mice in both syngeneic and T-cell receptor transgenic models. Transcriptome profiling, single cell sequencing, cytokine assays and T cell signaling analysis showed that Pdia3 editing in T cells enhances effector functions. Engineered PDIA3 mutant EGFRvIII chimeric antigen T cells are more potent in antigen-specific killing of human GBM cells.

Immunotherapy has offered transformative clinical benefits for diverse cancer types[1]. Checkpoint blockade enhances the antitumor response by neutralizing cytotoxic T lymphocyte–associated protein 4 (CTLA-4), programmed cell death protein 1 (PD-1) or its ligand PD-L1 (refs. [2–5]). However, for patients with GBM, the most common and deadliest primary malignant brain tumor in adults, checkpoint blockade efficacy is minimal. A recent clinical trial showed that PD-1 blockade does not prolong survival of patients with GBM (NCT02017717). Combination of anti-PD-1 and anti-CTLA-4 in patients with GBM failed to provide clinical benefits and engendered serious adverse effects[6]. EGFR-vIII chimeric antigen receptor (CAR)-T therapy evaluated in GBM clinical trials showed little overall survival benefit[7]. These clinical failures underscore the need to identify targets that enhance anti-tumor activity of CD8$^+$ T cells in GBM. Although genetic screens on human primary T cells are feasible, given the complexity of the GBM tumor microenvironment, it is important to carry out screens in an in vivo setting in hosts with intact immune systems. Efficient manipulation of mouse primary T cells may facilitate in vivo genetic screens directly on T cells in immunologically relevant animal models.

To further improve gene editing in murine primary T cells, we explored viral vectors and found that AAV is a potent carrier of CRISPR–Cas9 gene-editing components in primary murine immune cells (Supplementary Fig. 1a). However, unlike lentivirus commonly used for CRISPR screens, AAV is a nonintegrating virus, making readout of single guide RNA (sgRNA) libraries impractical, except a direct readout on target sites with targeted capture sequencing[8]. The limitation of capture sequencing is that the number of capturable targets limits the number of genes in a 'screenable' library, usually on the order of dozens to a few hundred[8,9]. We thus set out to develop more efficient tools for large-scale in vivo target discovery in otherwise difficult-to-edit murine primary T cells.

Here, we harness AAV–CRISPR and genomic integration of the transposon system to develop a hybrid genetic screening platform where CRISPR libraries are embedded in the *Sleeping Beauty* transposon carried between the inverted terminal repeats of AAV. This enables efficient gene editing in primary murine T cells and genomic integration of the sgRNA cassette for screen readout. We focused our screen on membrane targets for enhancement of CD8$^+$ T-cell activity, because membrane-bound proteins are amenable to monoclonal antibody (mAb)-based therapies, and their encoding genes can also be targeted by direct T-cell gene editing.

Results

Generation of AAV–SB–CRISPR hybrid vector and surface proteome knockout library. We generated a hybrid AAV vector for CRISPR perturbation of primary T cells that additionally uses a hyperactive *SB* transposon system, SB100x (ref. [10]). By AAV transduction,

[1]System Biology Institute, Integrated Science & Technology Center, West Haven, CT, USA. [2]Department of Genetics, Yale University School of Medicine, New Haven, CT, USA. [3]Center for Cancer Systems Biology, Integrated Science & Technology Center, West Haven, CT, USA. [4]Yale M.D.–Ph.D. Program, Yale University School of Medicine, New Haven, CT, USA. [5]Immunobiology Program, Yale University School of Medicine, New Haven, CT, USA. [6]Department of Immunobiology, Yale University School of Medicine, New Haven, CT, USA. [7]Department of Neurosurgery, Yale University School of Medicine, New Haven, CT, USA. [8]Yale Comprehensive Cancer Center, Yale University School of Medicine, New Haven, CT, USA. [9]Yale Stem Cell Center, Yale University School of Medicine, New Haven, CT, USA. [10]Yale Liver Center, Yale University School of Medicine, New Haven, CT, USA. [11]Yale Center for Biomedical Data Science, Yale University School of Medicine, New Haven, CT, USA. [12]These authors contributed equally: Lupeng Ye, Jonathan J. Park, Matthew B. Dong.
*e-mail: sidi.chen@yale.edu

the transgene can integrate into the genome thereby allowing direct sgRNA library readout, while simultaneously expressing sgRNA to allow gene editing, enhancing high-throughput screenability (Fig. 1a). We term this vector AAV–SB100x (AAV-Vector), and the hybrid system AAV–SB–CRISPR, hereafter. We generated AAV, transduced mouse primary naïve CD8$^+$ T cells and tested the genomic integration of AAV–SB100x using splinkerette PCR (see Methods and Supplementary Fig. 1b). Electrophoresis of the splinkerette PCR amplification products from AAV–SB100x-infected T cells, but not from uninfected T cells, showed multiple bands of varying intensity, indicating random genomic integration (see Methods and Supplementary Fig. 1c). We sequenced the splinkerette PCR products and revealed that they indeed mapped to the mouse genome with junctions to the *SB* transposon inverted repeats (Supplementary Fig. 1d). The genomic reads spanned across 18 of 19 autosomes and both sex chromosomes (X and Y) in the mouse genome (Supplementary Fig. 1e and Supplementary Dataset 1). Most of the integration sites mapped to intergenic regions and intronic regions, rather than promoters, coding regions or exonic untranslated regions (Supplementary Fig. 1f and Supplementary Dataset 1), suggesting that these random integrations rarely disrupt essential coding or key functional elements.

We designed a focused sgRNA library (mouse surface and membrane protein-encoding gene library, Surf), targeting 1,658 genes associated with the term 'cell surface', with 6,628 sgRNAs and 1,000 nontargeting controls (NTCs) (see Methods and Supplementary Table 1). We cloned Surf into AAV–SB100x vector (AAV–Surf) and verified successful cloning by sgRNA readout using Illumina sequencing (see Methods). We pool-packaged the AAV–Surf plasmid library into a viral library at a titer of approximately 1.4×10^{12} viral genome copies per milliliter (1.4×10^{12} vg ml^{-1}). While AAV titer estimated by genome copy is often high, functional transduction can be multiple orders of magnitudes lower due to empty viral particles, defective particles, noninfectious particles, nonproductive infections and clearance by host cells[11,12]. Therefore, we performed analysis of functional multiplicity of infection (MOI) via single cell sgRNA quantitative PCR (qPCR) of T cells, which were transduced with the AAV–Surf library for 5 d. Single cells with functional sgRNA expression are estimated at 48%, or a functional MOI of 0.65 (Supplementary Fig. 2).

In vivo AAV–Surf T-cell GBM screen identified robust hits. Considering the delicacy of the brain tumor microenvironment, we first performed primary T-cell screening in GBM using fully immunocompetent syngeneic models. We set up syngeneic mouse models with native or firefly luciferase-expressing GL261 cell lines (GL261 or GL261-Fluc/GL261-Luc) orthotopically transplanted into the lateral ventricle of C57BL/6J mice via intracranial injection using a stereotaxic instrument (Fig. 1a). With intracranial injection of GL261 or its derivatives, the penetrance of brain tumor induction in untreated mice is at or near 100% (Supplementary Fig. 3a,b). We isolated Cas9$^+$ naïve CD8$^+$ T cells from constitutive Cas9 mice (Rosa26-Cas9, or Cas9β, generated by crossing Rosa26-LSL-Cas9 to β-actin Cre driver[13]). We activated Cas9$^+$CD8$^+$ T cells with anti-CD3ε and anti-CD28, and transduced them with the AAV–Surf library to mutagenize the membrane proteome. CD8$^+$ T cells after 5 d in culture showed no difference between AAV–Surf and AAV–Vector groups in PD-1, Lag3 or Tim-3 (Supplementary Fig. 4a). Using CD45.1 transgenic mice, we were able to distinguish the donor T cells from those in the host (Fig. 1b). With CD8$^+$ T cells isolated from Cas9β;CD45.1 mice and transduced with AAV, we measured the number of infiltrated donor-derived CD8$^+$ T cells (Fig. 1c). It is interesting that mice from the AAV–Surf group have increased number of infiltrated T cells, potentially linked to enhanced trafficking and/or survival of certain mutant T cells, or more complicated cell–cell interactions with a complex mutant pool. These tumor-infiltrating lymphocytes (TILs) also have no difference in surface PD-1 level (Supplementary Fig. 4b,c). We performed T-cell receptor (TCR) sequencing on the pre-injection T cells and postinjection TILs, and observed a large number of different TCR clonotypes in pre-injection T cells as well as reduction of clonality in postinjection T cells, potentially due to limited number of TILs in the brain (Supplementary Fig. 4d–f and Supplementary Dataset 2).

We then performed adoptive transfer of the AAV–Surf pool mutant CD8$^+$ T cells into GBM-engrafted mice via tail vein injection (Fig. 1a). In parallel, we performed two independent screens using CD8$^+$ T cells from TCR transgenic mice (OT-I)[14] bred to Cas9β (OT-I;Cas9β) (Supplementary Fig. 5a). We monitored injected mice for brain tumor development by observation of macrocephaly and by in vivo luciferase imaging where GL261-FLuc cells were used (Supplementary Fig. 5b,c). Results showed that adoptive transfer of CD8$^+$ T cells increased overall survival (Supplementary Fig. 5d). Brain tumors were found in most mice at the endpoint (Supplementary Fig. 5e), except for three mice in the AAV–Surf group that were luciferase-negative after T-cell treatment.

Fig. 1 | In vivo AAV–SB-CRISPR CD8$^+$ T-cell screen of membrane proteome knockouts in GBM. a, Top, schematics of the hybrid AAV–SB–CRIPSR vector. Bottom, schematics of in vivo AAV–SB–CRIPSR screen in a syngeneic mouse model of GBM. Schematics of naïve CD8$^+$ T cell isolation, AAV library transduction, GBM cell transplantation, adoptive cell transfer, organ isolation, sgRNA readout and deep sequencing. GL261 cancer cells (5×10^5) were injected into the brain, and 3×10^6 Cas9β CD8$^+$ T cells were i.v. injected after 10 d of tumor engraftment. Brain tumors were dissected at the endpoint of survival. **b**, Flow cytometry analysis of TILs in the GBM-bearing brain. GL261-FLuc cancer cells (5×10^5) were injected per mouse; at day 12 after tumor injection, luciferase imaging was performed to reasonably group mice based on luminescence intensity; then 4×10^6 CD45.1$^+$;Cas9β CD8$^+$ T cells were i.v. injected. Mice were euthanized at day 6 after T cell injection; brains (without olfactory bulb and hindbrain) were dissected for TIL isolation. The i.v.-injected CD45.1$^+$;CD3$^+$;CD8$^+$ T cells were quantified and sorted for T cell receptor (TCR) sequencing. Cas9β mouse and CD45.1$^+$;Cas9β mouse splenocytes were used as gating controls. Data were collected from one experiment. **c**, Quantification of TIL number after transduction with AAV–Vector and AAV–Surf virus. Data were collected from two mice per group; two independent stainings were performed for each mouse. Data shown are mean ± s.e.m. *$P<0.05$, Mann Whitney test, two-tailed. **d**, Bulk analysis for brain tumor versus cell sgRNA library representation of an AAV–Surf GBM CD8$^+$ T-cell screen experiment. A list of most significantly enriched sgRNAs in brain tumors are highlighted as red dots (FDR ≤ 0.2%). Custom methods comparing sgRNAs with NTCs were used to estimate enriched sgRNAs (one-sided). FDR was calculated based on the ranks of sgRNAs relative to NTCs. **e**, RIGER analysis for brain tumor versus cell gene-level significance of AAV–Surf screen experiment, taking the metrics from multiple sgRNAs. The top ten most enriched genes (by RIGER *P* value, second-best sgRNA method) in brain tumors are highlighted. **f**, CD8$^+$ T cell mRNA levels of several top hits from the AAV–Surf GBM screen. The mRNA levels of all candidates were measured with RT–qPCR using gene-specific probes, indicating that all genes tested are expressed in mouse primary CD8$^+$ T cells ($n=3$ for *Gapdh*; $n=2$ for other genes). **g**,**h**, Nextera indel analysis for *Mgat5* and *Pdia3* knockout in mouse CD8$^+$ T cells. **g**, Representative mutations were shown around predicted sgRNA target sites. **h**, Quantification of total indel frequency for each gene was shown, demonstrating that AAV-mediated primary mouse CD8$^+$ T-cell gene editing was efficient. ($n=2$ for Vector group; $n=3$ for sgMgat5 and sgPdia3 groups). Data are shown as mean ± s.e.m., plus individual data points on the graph. IR, inverted repeat; DR, direct repeat; ITR, inverted terminal repeat; NTC, non-targeting control; GTS, gene-targeting sgRNA; WT, wild type.

Using barcoded primers (Supplementary Table 2) specific for AAV–SB100x, we performed sgRNA library readout (Supplementary Tables 3–5). The majority of the 1,000 NTC sgRNAs follow a linear regression line between brain and cell pellet (Fig. 1d) representing a null joint distribution without selection; whereas a fraction of sgRNAs are highly enriched in the brain, suggesting expansion of these specific mutant T cells (Fig. 1d). At a stringent false-discovery rate (FDR) of 0.2%, we identified 33 enriched sgRNAs targeting various membrane proteins, which include *Mgat5*, *Cdh11*, *Emp1*, *Lag3*, *Slc29a4*, *Rnpep*, *Hef2*, *P4ha1*, *Man2a1* and *Pdia3* (Fig. 1d). We performed RNAi gene enrichment ranking (RIGER) analysis for gene level significance (Methods), which showed *Mgat5*, *Pdia3*, *Pde5a*, *Ccdc80*, *Tnfrsf18*, *Defb26*, *Chrna7*, *Tspan13*, *Plat* and *Lag3* as the top ten hits (Fig. 1e). All top ten hits have two or more independent sgRNAs targeting different regions of the same genes ranking at the top 200 of 7,628 sgRNAs (Supplementary Table 6, $n=7$, RIGER 'second-best guide' algorithm), which makes it unlikely that such enrichment is simply mediated by off-target effects.

Lag3 is a well-known immune checkpoint regulator expressed on T cells[15–18] and a prime target for immunotherapy[5], currently with anti-LAG-3 mAb clinical trials for GBM (NCT02658981, NCT03493932). In two independent screens (one shorter term and one longer term) using an OT-I;Cas9β TCR transgenic system, we also identified highly similar lists of hits (Supplementary Fig. 5f,g). Mouse-to-mouse variation exists, which is even more challenging in the brain setting where the number of TILs per brain is limited.

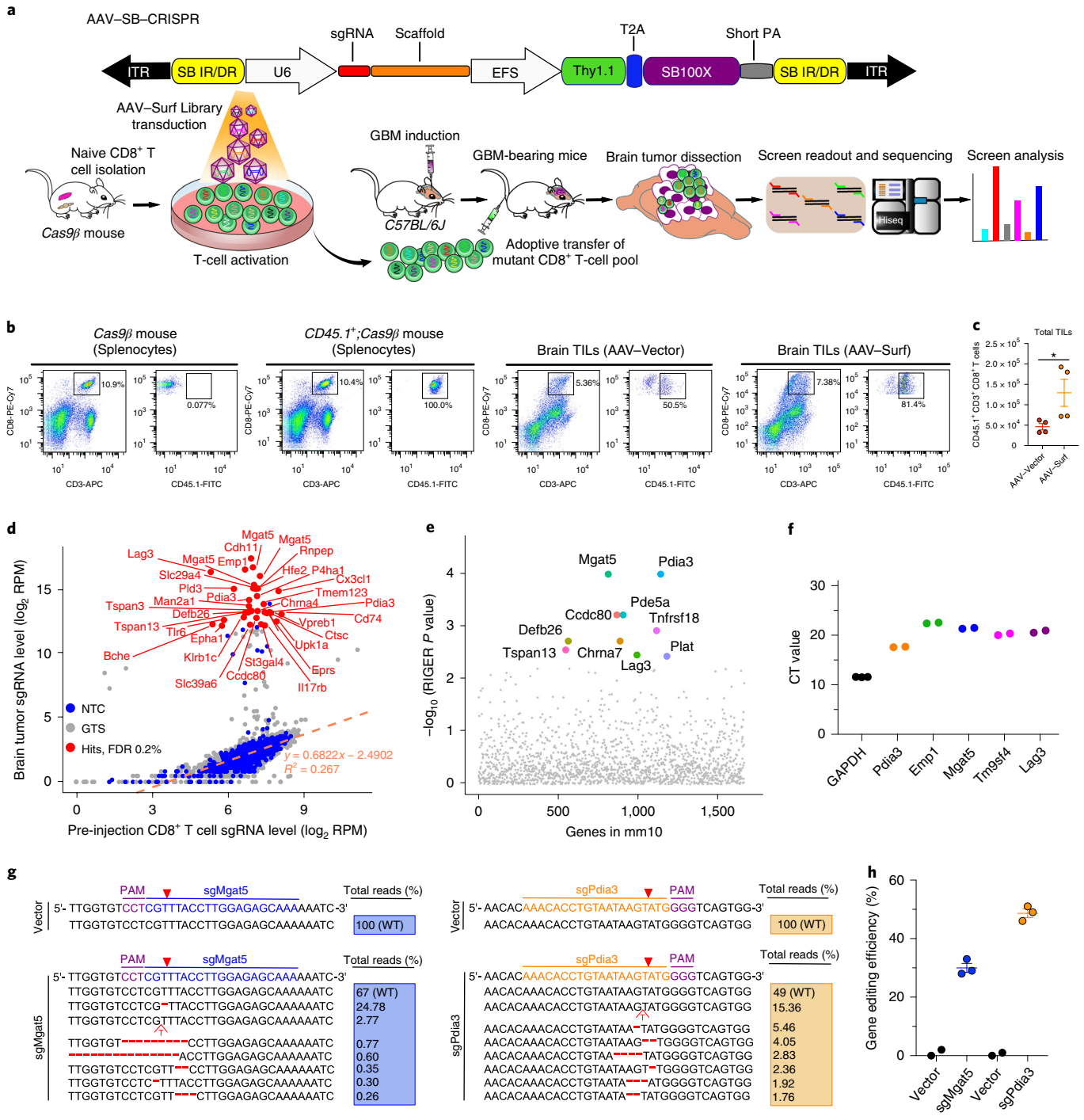

Therefore, we considered reproducibility among multiple animal replicates, multiple sgRNAs and multiple screens when choosing hits for further investigation. Notably, *Pdia3*, *Mgat5* and *Emp1* were among the top hits supported by multiple independent animals and/or multiple sgRNAs, across all three screens. We performed qPCR with reverse transcription (RT–qPCR) and confirmed that these hits are abundantly expressed in mouse CD8$^+$ T cells (Fig. 1f). We hypothesized that these genes may modulate T cell anti-tumor activity against GBM.

Preclinical efficacy testing of top hits by direct T-cell editing and adoptive transfer. Single gene-targeting sgRNAs showed that AAV–SB–CRISPR generated high-efficiency gene editing of *Pdia3* and *Mgat5* in mouse primary CD8$^+$ T cells (Fig. 1g,h). T7EI assay and RT–qPCR confirmed on-target gene editing and messenger RNA downregulation before T-cell adoptive transfer (Supplementary Fig. 6b,d). By surveyor assay, we found no editing in any of the top four predicted off-target sites by sgPdia3 (Supplementary Fig. 6c). In a syngeneic orthotopic GBM model with GL261 intracranial implantation in C57BL/6J mice, survival analysis of GBM-engrafted mice showed that the individual knockouts of each of the three genes (*Lag3*, *Mgat5* and *Pdia3*) in the adoptively transferred CD8$^+$ T cells prolonged overall survival when compared with AAV–Vector control (Supplementary Fig. 6e,f). We then used an antigen-specific OT-I;Cas9β CD8$^+$ T cell with transgenic TCR that recognizes GL261 brain tumors expressing a model antigen, chicken ovalbumin (cOVA). We established single cell-derived clonal GL261-FLuc-mCh-cOVA cell lines (Supplementary Fig. 6a). We transplanted GL261-FLuc-mCh-cOVA#1 cells into the lateral ventricles of *Rag1*$^{-/-}$ mice to induce GBM, then adoptively transferred single gene-edited or control OT-I;Cas9β CD8$^+$ T cells intravenously (i.v.) into GBM-bearing recipients (Fig. 2a). Survival analysis showed that AAV–CRISPR perturbation of *Mgat5*, *Pdia3* or *Emp1* improved overall survival of GL261-cOVA GBM-bearing mice when compared with AAV–Vector control (Fig. 2b). Furthermore, flow cytometry analysis of infiltrating CD45.2$^+$;CD8$^+$ immune cells revealed higher abundance of *Mgat5* and *Pdia3* knockout CD8$^+$ T cells following adoptive transfer (Fig. 2c). All animals developed brain tumors with the pathology of GBM (Supplementary Fig. 6g,h). These data suggested that single gene AAV–CRISPR perturbations of *Mgat5*, *Pdia3*, *Lag3* or *Emp1* enhanced the efficacy of adoptive T-cell transfer against GBM in mice with both immunocompetent and antigen-specific transgenic TCR models.

Validating efficacy of *Pdia3* and *Mgat5* perturbation in CD8$^+$ T cells using independent models. While i.v. delivery offers simplicity of infusion, it encounters hurdles such as lack of local concentration, or systemic side effects. Intracranial infusion is a local delivery that avoids potential systemic toxicity, although with different complications or caveats. GBM therapy naturally involves surgical procedures, and intracranial T-cell therapy has entered clinical trials for recurrent GBM (NCT03283631). Bearing in mind its advantages and caveats, we tested intracranial adoptive transfer of the CRISPR-perturbed T cells. We injected 5×10^5 GL261-FLuc cells via intracranial procedure to induce tumor (Fig. 2a). Because of the complete penetrance of this model (Supplementary Fig. 3a,b), it is expected that all mice will develop brain tumors with this number of cells injected. At 14 d post brain tumor challenge, we performed intracranial injection of AAV–sgMgat5 or AAV–sgPdia3 virus-infected CD8$^+$ T cells at 1:1 initial seeding ratio (cancer cell/T cell) into the lateral ventricle of tumor-bearing mouse brains (Fig. 2a). Luciferase imaging showed disease progression (Fig. 2d and Supplementary Fig. 7a), and mice receiving *Mgat5* or *Pdia3* knockout CD8$^+$ T cells had substantially improved overall survival (Fig. 2e). We repeated the intracranial adoptive T-cell transfer experiment with a lower cancer cell/T cell initial seeding ratio (1:7.5) (Fig. 2f). Of note, because of the variable kinetics of the number of animals deemed for euthanasia, we noted that the quantifications are not comparable between groups at later time points when a number of mice were euthanized (Supplementary Fig. 7b). All mice receiving AAV–Vector-infected CD8$^+$ T cells quickly reached survival endpoints due to rapid GBM progression (Fig. 2f,g), whereas all three AAV–CRISPR CD8$^+$ T-cell perturbation groups had prolonged survival (AAV–sgMgat5, AAV–sgPdia3 or AAV–sgMgat5 + AAV–sgPdia3), with a fraction of mice becoming tumor-free and having long-term survival (Fig. 2f,g). We examined the brains of long-term survivor mice by histology at 8 months (approximately 240 d) postinjection and found that their brains were indeed tumor-free (Fig. 2h). These data suggest that single gene AAV–CRISPR perturbation of *Mgat5*, *Pdia3* or their combination enhanced the efficacy of intracranial adoptive T-cell transfer against GBM.

Fig. 2 | In vivo validation of top candidates by adoptive transfer of mutant CD8$^+$ T cells in mouse models of GBM. a, Schematic of the preclinical therapeutic efficacy testing strategy for top candidates from the AAV-Surf screens using an independent model of GBM immunotherapy, where cancer cells express a cognate cOVA model tumor antigen recognized by CD8$^+$T cells from TCR transgenic *OT-I* mice. A syngeneic mouse model of GBM was used to evaluate therapeutic efficacy by intracranially (i.c.) delivering T cells. **b**, Survival plots of adoptive transfer top candidate validations in *Rag1*$^{-/-}$ mice. *Mgat5*, *Pdia3* and *Emp1* were chosen for gene editing in CD8$^+$T cells for therapeutic efficacy testing. All mice were engrafted with 1×10^5 GL261-FLuc-mCh-cOVA cells, and adoptive transfer was performed after 10 d of tumor engraftment by i.v. injection of 1×10^6 OT-I;Cas9β CD8$^+$T cells infected with AAV-Vector ($n=8$), AAV-sgMgat5 ($n=10$), AAV-sgPdia3 ($n=9$) and AAV-sgEmp1 ($n=8$). Vector control from the same group and each gene was plotted against Vector separately for visibility. Survival significance was assessed by a log-rank Mantel–Cox test. **c**, Dot plot of quantitative results for CD45.2$^+$ and CD8$^+$ CD8$^+$ T-cell infiltration in GBM-bearing mice (TILs) with or without *Mgat5* or *Pdia3* knockout ($n=3$ for each group). Unpaired *t*-test was used to assess significance. $^*P<0.05$. Data are shown as mean ± s.e.m., plus individual data points on the bar graph. **d**, Representative IVIS images. In vivo imaging illustrates that all mouse brains had a growing tumor at day 12. The luciferase imaging was performed every 2 d using an IVIS system. The tumor growth rate slowed down after injecting T cells infected with AAV-sgMgat5 or AAV-sgPdia3 virus compared with the AAV-Vector group. Data were collected from one independent experiment; each group included five to eight mice. **e**, Survival plots of mice treated with T cells. Survival significance was assessed by a log-rank Mantel–Cox test. DPI, days post tumor implantation. **f**, Top, a time line for tumor induction, T-cell i.c. injection and imaging for therapeutic efficacy testing of AAV-SB-CRISPR targeting *Pdia3*, *Mgat5* and combination in CD8$^+$ T cells in a syngeneic mouse model of GBM. C57BL/6J mice were implanted i.c. with 2×10^5 GL261-FLuc cancer cells on day 0. In vivo imaging was performed at day 14 before T-cell injection for randomization with tumor-burden-matched subgrouping. T cells (1.5×10^6) were injected i.c. at the same coordinate as tumor injection. The luciferase imaging was performed every 2–3 d. Bottom, representative IVIS images of brain tumor growth in GL261-FLuc cancer cell-injected mice receiving i.c. injection of T cells infected with AAV-Vector, AAV-sgMgat5 and AAV-sgPdia3 virus groups. Data were collected from one independent experiment; each group had seven to eight mice. **g**, Survival plot of mice treated with T cells. Overall survival significance was assessed by a log-rank Mantel–Cox test between Vector and mutant groups. Comparison between groups, log-rank test. **h**, Whole brain section hematoxylin and eosin staining of four long-term survivor mice. Scale bar, 2 mm for whole brain sections. Data were collected from one independent experiment; survivor mice were from the same experiment as in **f** and **g**. The *P* values and numbers of mice used in each group are indicated in the plots and/or in Source Data. d, day.

Enhanced anti-tumor activity of *Pdia3* mutant CD8 T cells. We performed single cell RNA sequencing (scRNA-seq) and profiled the transcriptomes of a total of 9,193 single CD8 T cells (Fig. 3a, Supplementary Fig. 8a and Supplementary Dataset 3). Comparing AAV–sgPdia3 with AAV–Vector-treated groups showed that *Pdia3* was substantially downregulated (Fig. 3b and Supplementary Fig. 8b), indicating a clear on-target effect. To our surprise, multiple effector cytokines are upregulated after *Pdia3* knockout. The top 5 upregulated genes are *Granzyme a (Gzma)*, *S100a6*, *Gzmb*, *Gzmc* and *Usmg5* (Fig. 3b and Supplementary Fig. 8b), which implied that granzyme family upregulation may account for the *Pdia3* mutant CD8$^+$ T cells' augmented ability to kill tumor cells.

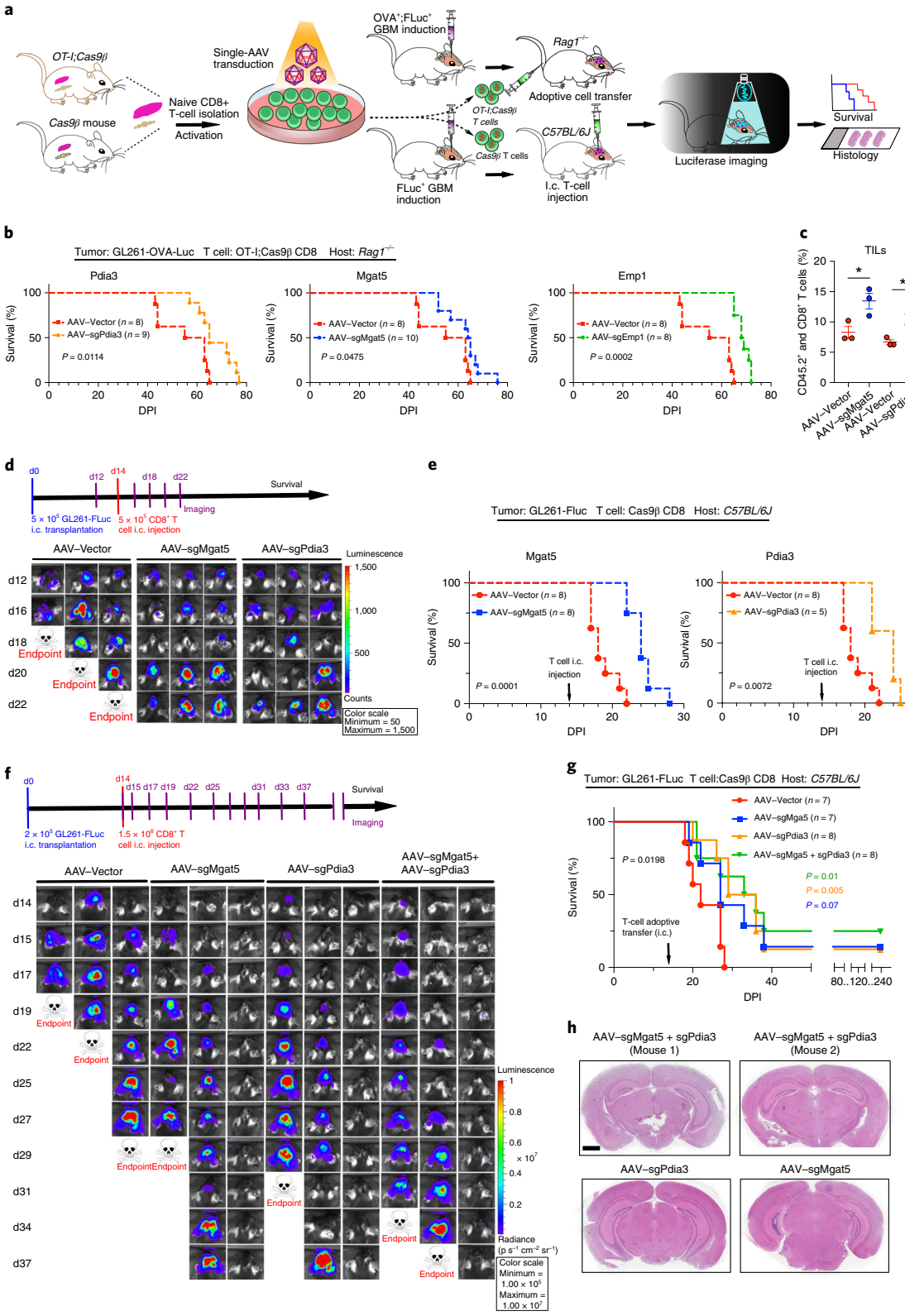

To show the bulk differences while minimizing other heterogeneous effects, we also performed transcriptome profiling of AAV–sgPdia3 and AAV–Vector-treated CD8+ T cells by bulk mRNA sequencing (mRNA-seq) (see Methods and Supplementary Dataset 4). Differential expression analysis revealed a striking set of differentially expressed genes between *Pdia3* knockout and control CD8+ T cells, with 1,365 genes upregulated and 555 genes downregulated at FDR-adjusted *Q* value < 0.001 (Fig. 3c and Supplementary Datasets 5 and 6). Gene set and pathway analyses revealed a strong signature of T-cell effector and pro-inflammatory immune gene upregulation on *Pdia3* knockout in CD8+ T cells (Fig. 3c,d and Supplementary Dataset 4). These include genes encoding T-cell effector cytokines (*Gzma/b/c/e/f/g*, *Perforin*, *Tnf*, *Ifng*), inflammatory cytokines and their receptors (*IL-10/13/22/23a*, *Ccl-1/3/4/5/9*, *Ccr8*), as well as costimulatory or activation receptors and their ligands (*Cd40lg*, *Tnfsf4/Ox40l*, *Tnfsf14/Light*, *Tnfrsf4/Ox40r*, *Tnfrsf18/Gitr*, *Tnfrsf10b/Trail*) (Fig. 3d). These transcriptome profiles showed that *Pdia3* knockout enhanced effector phenotypes in CD8+ T cells.

We performed RT–qPCR to validate the RNA-seq results, which confirmed the upregulation of granzyme genes on AAV–sgPdia3 perturbation (Fig. 3e). To further exclude off-target factors, we validated the result using two independent sgRNAs targeting different regions of the *Pdia3* gene (Fig. 3f). It was shown that *Mgat5*-deficient T cells augment phosphorylation of Plcγ and Erk, critical molecules required for T-cell activation[19–21]. We investigated T-cell signaling pathways on *Pdia3* perturbation. Quantification of immunoblots showed that the phosphorylation of Plcγ and Erk1/2 was upregulated across a dose-dependent anti-CD3ε stimulation (Fig. 4a,b). In concordance with the more sensitive TCR signaling pathway, intracellular flow cytometry experiments revealed that Ifnγ production was upregulated in AAV–sgPdia3-infected CD8 T cells, which secreted more Ifnγ with low anti-CD3ε stimulation (Fig. 4c,d). This was again validated using an independent sgRNA targeting *Pdia3* (Fig. 4e). Collectively, these data suggest that inhibition of *Pdia3* led to upregulation of granzyme gene expression and a more sensitive induction threshold for TCR signaling and Ifnγ production.

Anti-tumor efficacy of *Pdia3* editing in CD8+ T cells in mouse tumor models. Because granzymes and Ifnγ are T-cell intrinsic properties, we speculated that *Pdia3* editing could also have anti-tumor effects in other models. We performed experiments using two independent models of antigen-specific orthotopic tumor immunotherapy. First, we induced GL261 tumors with subcutaneous injection, and treated the tumor-bearing mice by adoptive transfer of mutant CD8+ T cells via i.v. injection (Fig. 4f). Knocking out *Pdia3* using AAV–sgPdia3 in CD8+ T cells enhanced the anti-tumor effect (Fig. 4g). Second, we used a different cancer cell line, E0771 (ref. [22]), to induce syngeneic orthotopic triple-negative breast cancer (TNBC) via mammary fat pad injection, and treated the tumor-bearing mice by T-cell adoptive transfer (Fig. 4f,h). PBS-treated TNBC grew aggressively to >2,000 cubic-mm in 3 weeks; Vector T-cell adoptive transfer controlled the tumor growth and *Pdia3* knockout in T cells further enhanced the efficacy (Fig. 4h). Together, these data suggest that the enhanced anti-tumor activity of *Pdia3* perturbation encompasses, at least in part, T-cell intrinsic phenotypes.

Mass cytometry (CyTOF) analysis of *PDIA3* knockout in human CD8+ T cells. To investigate *PDIA3* in human CD8+ T cells, we generated high-efficiency editing of *PDIA3* in human CD8+ T cells using Cas9 ribonucleoprotein (RNP) (Fig. 5a–e). DNA level analyses by surveyor assay and Nextera next generation sequencing demonstrated that *PDIA3* knockout was highly efficient (86%) (Fig. 5b–d). Western blot using an antibody specific to human PDIA3 showed 92% protein level knockdown in crPDIA3-treated T cells (Fig. 5e). We performed anti-CD3 dose-dependent analysis of IFNγ production and found that *PDIA3*-edited CD8+ T cells had higher IFNγ (Fig. 5f,g). RT–qPCR analysis of human *GZMA* also showed upregulation on *PDIA3* loss (Fig. 5h).

Next, we performed mass cytometry (cytometry by time of flight, CyTOF) and profiled multiple immune markers in a total of 227,848 single cells (Supplementary Fig. 9a,b), which mapped the high-dimensional landscapes of multiple immune checkpoints and other functional molecules in *PDIA3* knockout and wild-type human CD8+ T cells. Clustering analysis showed that the three PDIA3 knockout samples clustered together and were distinct from the three wild-type samples (Supplementary Fig. 9a,b), revealing the consistency of datasets. Perforin, costimulation markers OX40/CD134 and ICOS/CD278, as well as CXCR3, were upregulated in *PDIA3* knockout T cells (Fig. 5i and Supplementary Fig. 9c). 4-1BB/CD137 and IL7R/CD127 were moderately altered, but not Fas/CD95 (Supplementary Fig. 9c). Interestingly, TIM-3 was upregulated in *PDIA3* knockout, consistent with mRNA-seq (Supplementary Fig. 9c). Together, these data showed that *PDIA3* CRISPR editing influenced the surface expression of multiple immune regulators and effectors in human CD8+ T cells.

Analysis of *PDIA3*'s cytotoxic T lymphocyte (CTL) signature with human clinical data. To investigate whether *PDIA3* expression was clinically relevant, we performed patient data analysis using the tumor immune dysfunction and exclusion (TIDE) algorithm (see Methods). *PDIA3* expression has strong signatures in CTL dysfunction, where PDIA3-low patient groups have CTL-associated overall survival benefits across multiple cancer types including GBM, TNBC and lung adenocarcinoma, while high-level *PDIA3* abolishes or weakens the overall survival benefit of CTL-high patients (Supplementary Fig. 10a–c). In patients with melanoma treated with immune checkpoint blockade antibodies, *PDIA3*-high patients had poorer survival (Supplementary Fig. 10d), although checkpoint antibodies are not yet commonly used for treating GBM. These data pointed to the significance of clinical association of *PDIA3* with T-cell dysfunction in human cancer.

***PDIA3* engineering enhanced CAR-T killing of human EGFRvIII+ GBM cells.** To further establish PDIA3 as an immunotherapy target of T-cell engineering, especially against GBM, we established *PDIA3*

Fig. 3 | Single-cell RNA-seq and bulk mRNA-seq analysis of *Pdia3* knockout in CD8+ T cells. a, t-SNE plot of sample distribution based on the transcriptome of 9,193 single cells from AAV–sgPdia3- and AAV–Vector-treated CD8+ T cells. **b**, Bubble-rank plot of differential gene expression of scRNA-seq. Delta-mean is the difference of mean expression value between AAV–sgPdia3 and AAV–Vector-treated single CD8+ T cells ($n = 3$ each group). Differential expression: two-sided Wilcoxon signed-rank test by gene, with *P* values adjusted using the Benjamini and Hochberg method. Statistical significance is scaled by $-\log_{10}$, *P* value as shown in the size key. **c**, A volcano plot of all differentially expressed genes between AAV–Vector and AAV–sgPdia3 transduced mouse primary CD8+ T cells ($n = 3$ biological replicates). Differential gene expression was performed with Sleuth using Wald test; the FDR-adjusted *Q* value was used for the plot. **d**, Heatmap of representative immune-related differentially expressed genes between AAV–Vector and AAV–sgPdia3 transduced mouse primary CD8+ T cells ($n = 3$ biological replicates). **e**, RT–qPCR validation of the scRNA-seq and bulk mRNA-seq results confirmed the upregulation of granzyme genes on AAV–sgPdia3 perturbation ($n = 4$). Unpaired *t*-test, two-tailed. $^{*}P < 0.05$, $^{****}P < 0.0001$. **f**, RT–qPCR validation of scRNA-seq and bulk mRNA-seq results using two independent *Pdia3* sgRNAs ($n = 3$). Unpaired *t*-test, two-tailed. $^{*}P < 0.05$, $^{**}P < 0.01$, $^{***}P < 0.001$, $^{****}P < 0.0001$. The *P* values and number of mice used in each group are indicated in the plots and/or in Source Data.

mutant and control human EGFRvIII CAR-T cells by Cas9-RNP-mediated gene editing of primary CD8+ T cells, along with AAV donor-mediated knock-in of an EGFRvIII CAR-T cassette into the TCR Alpha Constant chain (*TRAC*) locus (see Methods and Fig. 6a). We also generated an EGFRvIII-antigen-expressing U87 GBM cell line (U87-Luc-EGFRvIII). We then cocultured CAR-T cells with cancer cells to test the cytolytic (killing) activity. *PDIA3* knockout compared with wild-type EGFRvIII CAR-T cells had higher killing ability against the cognate U87-Luc-EGFRvIII cells (Fig. 6b). This was confirmed using an independent sgRNA targeting *PDIA3* (Fig. 6c), further minimizing the probability of off-target effects. The killing ability of CAR-T is similar between

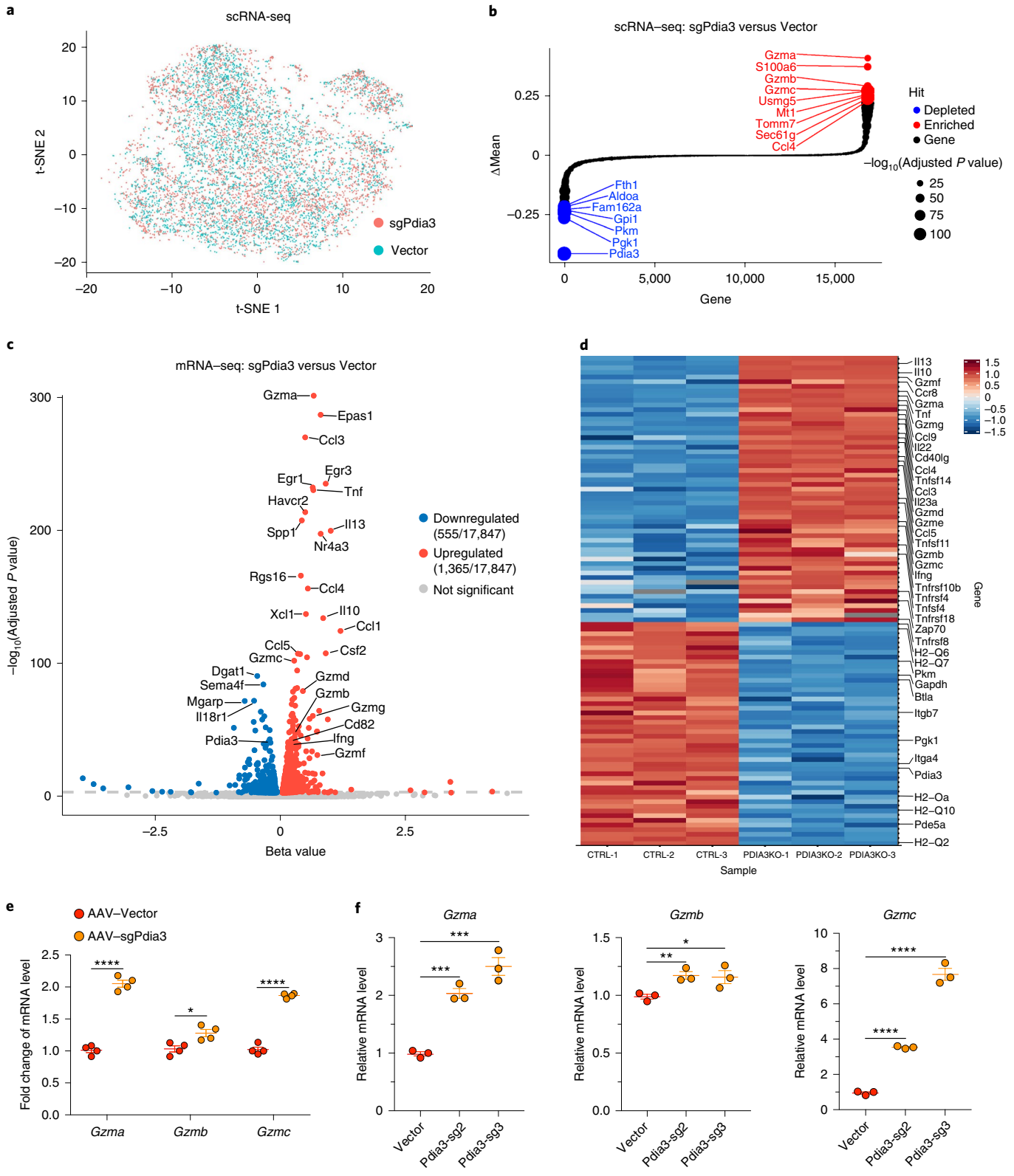

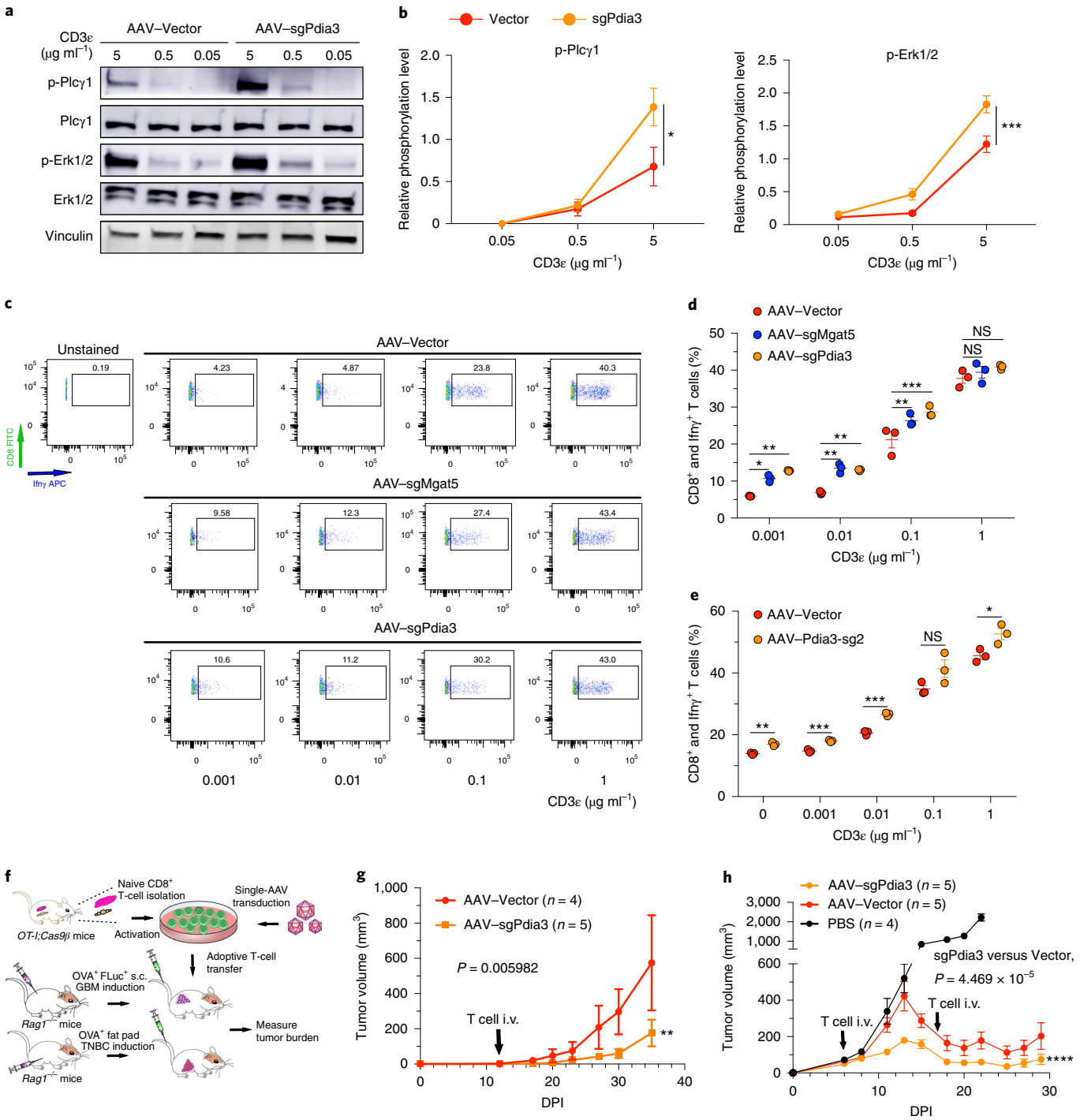

Fig. 4 | Mechanistic analysis and preclinical efficacy testing of *Pdia3* knockout in CD8⁺ T cells. a,**b**, Dose-dependent TCR signaling experiment for *Pdia3* knockout showing upregulation of the phosphorylation levels of Plcγ and Erk1/2. **a**, Original western blot gel of a representative experiment among the three independent replicate experiments. **b**, Quantification of relative phosphorylation levels of Plcγ and Erk1/2 ($n = 3$). Data are shown as mean ± s.e.m. Two-way analysis of variance (ANOVA), sgPdia3 versus vector, $^{*}P < 0.05$, $^{***}P < 0.001$. **c**–**e**, Intracellular flow cytometry was performed to detect the expression levels of Ifnγ. The OT-I;Cas9β CD8⁺ T cells were infected with AAV-Vector and AAV-sgMgat5 or AAV-sgPdia3 after isolation. Before Ifnγ detection assay, T cells were rested for 12 h, then reactivated with a different concentration of anti-CD3ε for 4 h. **c**, Flow cytometry results suggested that *Mgat5* or *Pdia3* knockout improved T-cell sensitivity to the low-concentration anti-CD3ε and secreted more Ifnγ. **d**, The quantification result of **c**. **e**, Ifnγ intracellular staining after *Pdia3* knockout using a different sgRNA. Two-sided multiple *t*-test was used to assess the significance; Holm–Sidak method was used for multiple comparisons correction. $^{*}P < 0.05$, $^{**}P < 0.01$, $^{***}P < 0.001$. NS, not significant. **f**, Schematic of the therapeutic efficacy testing strategy for *Pdia3* knockout T cells using a subcutaneous model of GBM and a syngeneic TNBC model. **g**, Tumor growth curves of GL261-FLuc-mCh-cOVA tumor bearing mice receiving T cells infected with AAV-Vector ($n = 4$) or AAV-sgPdia3 ($n = 5$). Wilcoxon rank sum test with continuity correction, two sided, $P = 0.005982$. **h**, Tumor growth curves of E0771-mCh-cOVA TNBC-bearing mice receiving CD8⁺ T-cell therapy. Wilcox test, two sided, using only data points on or after T-cell adoptive transfer: AAV-Vector versus AAV-sgPdia3, $P < 0.001$. The *P* values and number of mice used in each group are indicated in the plots and/or in Source Data.

PDIA3 mutant and control towards the parental U87 cells without EGFRvIII antigen (Fig. 6d), supporting CAR-T's antigen specificity. These data together demonstrate that the major effect of *PDIA3* knockout in EGFRvIII CAR-T cells is dependent on CAR-antigen recognition, and minimally due to TCR off-target or gene editing off-target effects.

Discussion

There are only four approved drugs for GBM to date, and none of these are immunotherapies. The brain is highly immune-privileged, with the exception of the meningeal lymphatic system[23]. Recent studies demonstrated active adaptive immune cell trafficking in the brain in the arachnoid meninges and dura, leptomeninges, cerebrospinal fluid and the central nervous system parenchyma[24]. The active brain surveillance by the adaptive immune system may provide a new window to identify targets that modulate T-cell function against GBM. The US Food and Drug Administration has approved checkpoint antibodies against PD-1/PD-L1 and CTLA-4 for various cancer types[1,5,25,26]. Although clinical trials with checkpoint inhibitors have entered the GBM clinic both as mono-therapy and as combinations[27], the efficacy and survival benefits are limited, except in a recent trial using anti-PD-1 in a neoadjuvant setting[28]. GBM typically has low mutational load and T-cell infiltration, possibly making it less responsive to checkpoint blockade[29]. Anti-PD-1 antibody (nivolumab) did not improve overall survival compared with bevacizumab in patients with recurrent GBM in a recent trial[30]. Combination of nivolumab and ipilimumab (anti-CTLA-4) treatment resulted in severe toxicity in 50% of patients with GBM[6], leading to discontinuation. Clinical trials with LAG-3 mAbs either alone or in combinations are ongoing (NCT02658981, NCT03493932). Several preclinical studies showed promise with various other forms of immunotherapies in GBM, such as granulocyte-macrophage colony-stimulating factor–expressing whole-glioma-cell vaccination and CTLA-4 blockade[31,32]; local chemotherapy with anti-PD-1 (ref. [33]); a triple combination of anti-CTLA-4, anti-PD-1 and oHSV G47Δ expressing murine IL-12 (G47Δ-mIL12)[34]; as well as dual PD-1 and TIM-3 blockade with radiation[35]. In summary, limited clinical efficacy and high toxicity remain unresolved problems for combinatorial checkpoint blockade immunotherapy in GBM.

CAR-T-cell therapy is recently approved by the Food and Drug Administration for refractory pre-B-cell acute lymphoblastic leukemia and diffuse large B-cell lymphoma. However, in solid tumors, currently available CAR-Ts alone most often showed insufficient single agent activity[36]. EGFR-vIII CAR-T has completed several clinical trials, yet has shown little overall survival benefit for patients with GBM[7]. Intracranial infusion of CAR-T cells targeting IL-13Rα2 against GBM initially showed tumor regression although with ultimate recurrence[37]. A ten-patient trial with recurrent EGFRvIII-positive GBM, with patients receiving a single i.v. infusion of autologous anti-EGFRvIII CAR-T cells, did not improve overall survival[7]. Recent preclinical studies have developed a number of promising GBM CARs, including those targeting chondroitin sulfate proteoglycan (CSPG4)[38], such as the disialoganglioside GD2 (ref. [39]). Therefore, improvements of CAR-T efficacy in GBM and solid tumors are critically needed. AAV–SB–CRISPR screens may facilitate rapid identification of novel factors modulating T-cell function to provide direct targets to enhance CAR-T efficacy. Our coculture model showed that *PDIA3* editing can enhance the killing ability of human CAR-T cells against EGFRvIII$^+$ GBM cells, while in vivo efficacy has yet to be determined.

Functional genetic screens can discover diagnostic markers and therapeutic targets[40]. A study using an immortalized T-cell line screened for regulators of PD-1 expression[41]. In vitro screens were reported in primary human T cells[42,43]. Genetic screens of human T cells in tumor models require immunodeficient mice. Screening in primary murine T cells offers the advantage of unbiased discovery of genes that modulate immune function in immunocompetent settings using syngeneic tumor models. RNA interference (RNAi) T-cell screens identified genes for T-cell infiltration and cytokine production[44,45]. CRISPR-based approaches demonstrated superior performance in head-to-head comparisons[46] such as higher consistency, lower off-target rate and fewer false negatives. We developed a hybrid AAV–SB–CRISPR system, which combines the power of AAV for transduction and transposon for genomic integration, enabling efficient genome editing of murine T cells, and empowers large-scale knockout screens in vivo. We screened a focused membrane proteome in CD8$^+$ T cells in syngeneic models of GBM in immunocompetent mice, and identified and validated previously uncharacterized targets across several GBM models. Among top hits, *Lag3* encodes an important cell-surface immune checkpoint. *Mgat5* has been shown to negatively regulate T-cell activation[47] and *Mgat5* knockout mice are tumor resistant[48]. Scoring these genes benchmarked the success of the screens. We validated the preclinical efficacy of *Lag3* and *Mgat5* in this study in a GBM model, together with *Pdia3* and *Emp1*, which have not been previously investigated in T cells or GBM. We performed studies with both immunocompetent B6 and antigen-specific OT-I/*Rag1*$^{-/-}$ settings, and carried out adoptive transfer via i.v. as well as intracranial approaches, although these were not in head-to-head comparisons. Nevertheless, these experiments demonstrate in a convergent manner that genetic perturbation of these targets enhanced anti-GBM efficacy. Our characterization experiments provided data on the previously unknown roles of PDIA3 in immune regulation and immuno-oncology-relevant phenotypes in CD8 T cells.

Finally, AAV–SB–CRISPR-mediated in vivo screens of membrane protein-coding genes are advantageous because the hits can serve as immuno-oncology targets either via mAbs or via direct T-cell engineering. While therapeutic-grade mAbs may require

Fig. 5 | Human CD8$^+$ T-cell PDIA3 knockout and effector function analysis. a, Schematics of human CD8$^+$ T-cell isolation, culture, RNP electroporation, T7EI assay, Nextera sequencing, flow cytometry and CyTOF analysis. **b**, T7EI assay showed human *PDIA3* knockout (KO) with a high efficiency compared with control. Arrows point to pre- and postcleavage products of predicted sizes. Data shown are representative of three independent experiments. **c**, Nextera data quantification of gene editing efficiency of **b**. **d**, Quantification of Nextera data ($n=2$ each). **e**, Western blot for PDIA3 change in protein level on CRISPR KO. Data from one experiment. **f**, IFNγ intracellular staining after *PDIA3* KO. **g**, Quantification of **f**. Two-sided multiple *t*-test was used to assess the significance. Holm–Sidak method was used for multiple comparisons correction. $^*P<0.05$, $^{**}P<0.01$. The *P* values and number of mice used in each group are indicated in the plots and/or in Source Data. **h**, qPCR validation of *GZMA* expression. Unpaired *t*-test, two-tailed. $^{***}P<0.001$. **i**, t-SNE plots of representative markers detected by the CyTOF. Perforin, two costimulatory molecules (CD134/OX40 and CD278/ICOS) and CXCR3 were upregulated at the single-cell level on *PDIA3* KO ($n=3$ replicates each; sampled 7,000 cells per replicate for comparison). Violin plots were used for visualizing marker levels quantitatively in single cells. Violins show kernel probability density on side, and boxplot is standard; that is, the middle band is median, hinges/ends of box are interquartile range (25 and 75% quantiles), lower whisker = smallest observation greater than or equal to lower hinge − 1.5 × interquartile range, upper whisker = largest observation less than or equal to upper hinge + 1.5 × interquartile range. Wilcoxon test, two-sided, *P* value adjusted by Benjamini and Hochberg method. KO versus WT, PERFORIN, $P=1.35\times10^{-294}$; CD278, $P=0$ (below algorithm detection limit); CD134, $P=0$; CXCR3, $P=0$. bp, base pair; CTRL, control.

multiple years of effort, direct T-cell engineering can enhance the efficacy of cell therapies such as CAR-T, T-cell receptor–engineered T-cell therapy (TCR-T) and TIL adoptive transfer. Albeit with limitations, targeting *PDIA3* and other genes via genome engineering of T cells also avoids toxicity issues due to target expression in other cell types. CAR-T-cell therapy faces various challenges including persistence in vivo, resistance to immunosuppression and exhaustion, all of which are critical for in vivo efficacy and potential clinical success. Genetic screens in CD4 T cells or other immune cell types may be performed similarly in the future. Direct editing or pharmacological perturbation of PDIA3 or other targets identified from these screens may provide different routes for improving T-cell-based immunotherapy for GBM and potentially more broadly for other difficult-to-treat cancer types.

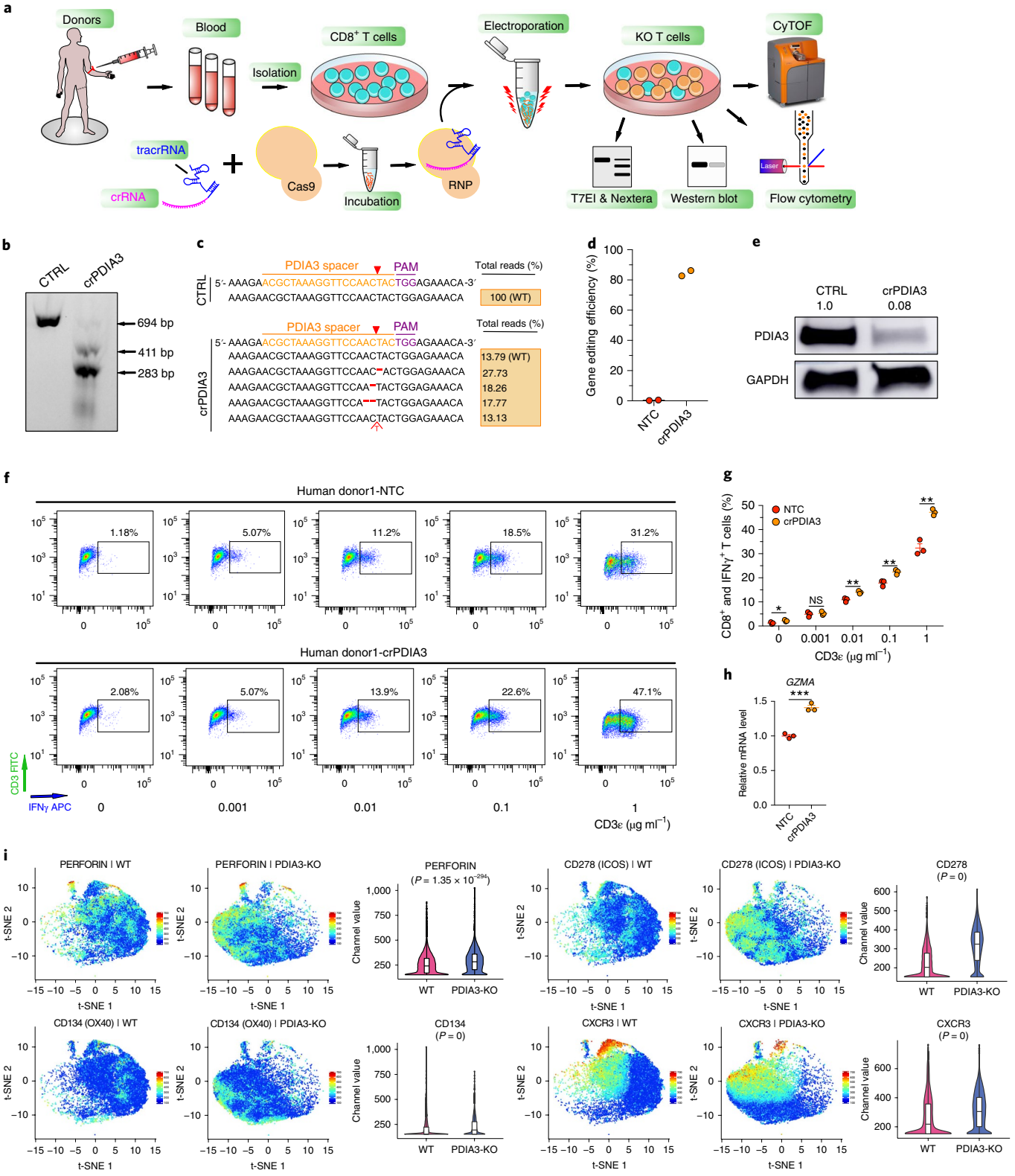

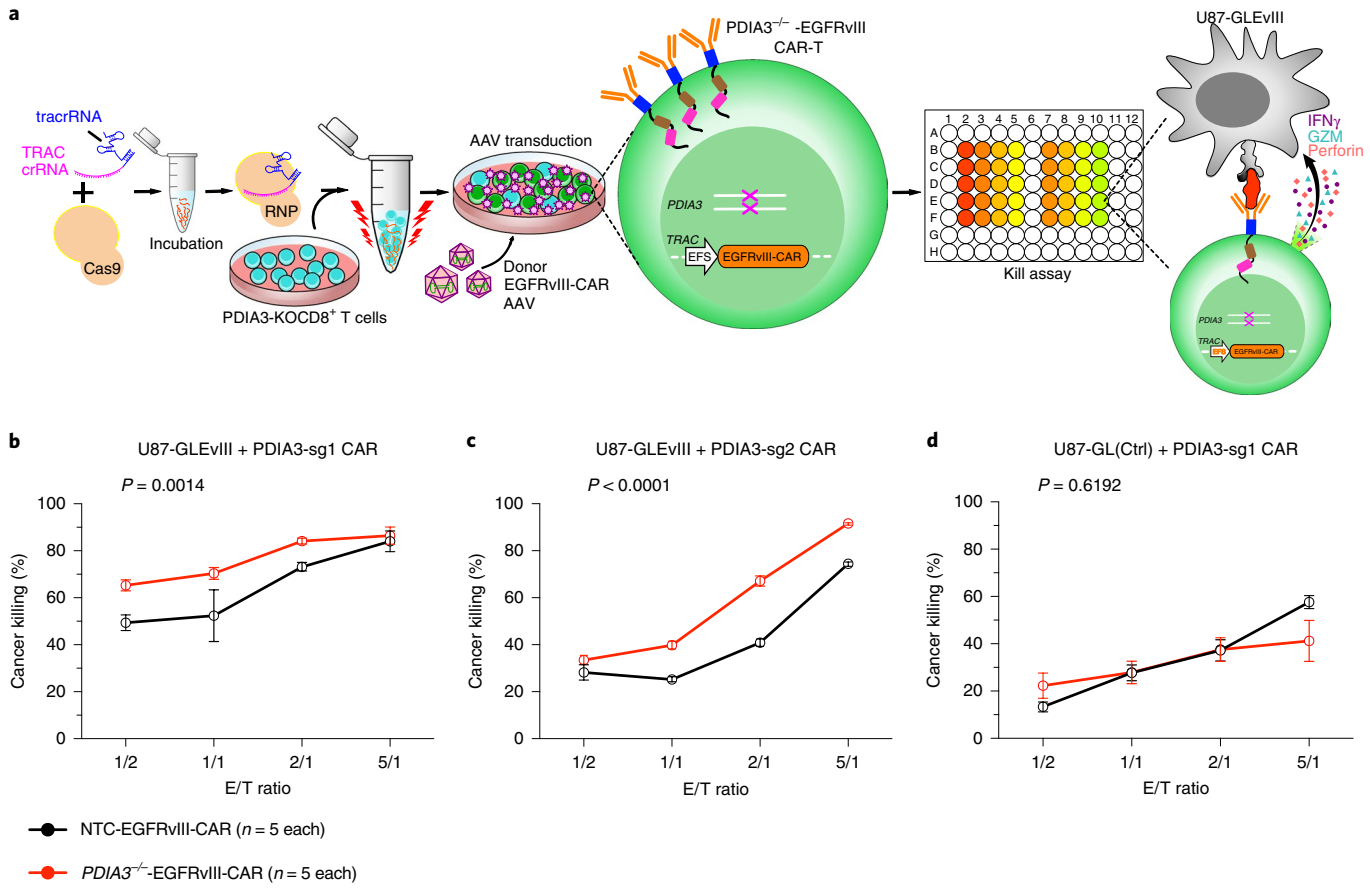

Fig. 6 | Human *PDIA3*$^{-/-}$-EGFRvIII CAR-T-cell establishment and GBM cell killing. a, Schematics of human *PDIA3*$^{-/-}$-EGFRvIII CAR-T-cell generation. CD8 T cells were first electroporated with crPDIA3:tracRNA:Cas9. Then *PDIA3*$^{-/-}$ T cells were knocked-in with an EGFRvIII-CAR construct which consists of *TRAC* locus homology-directed repair 5′ and 3′ arms, an EFS promoter, an EGFRvIII-CAR expression cassette and a short poly(A). The donor knock-in constructs were packaged into AAV6, then introduced into T cells by viral transduction after electroporation of RNP targeting the first exon of *TRAC*. U87-GFP-Luc-EGFRvIII (U87-GLEvIII) and *PDIA3*$^{-/-}$-EGFRvIII CAR-T-cell coculture (kill) assay was set up after CAR-T cells were established to test *PDIA3*$^{-/-}$-EGFRvIII CAR-T-cell killing ability. **b**–**d**, Kill assay of NTC-EGFRvIII-CAR and *PDIA3*$^{-/-}$-EGFRvIII-CAR T cells with U87-GLEvIII and U87-GL (parental line control) human GBM cells, with a titration series of effector/target (E/T) ratios at 24 h post coculture. **b**, Kill assay with PDIA3-sg1, on U87-GLEvIII cells. **c**, Kill assay with PDIA3-sg2, on U87-GLEvIII cells. **d**, Kill assay with PDIA3-sg1, on U87-GL parental control cells. Data are shown as mean ± s.e.m., plus individual data points, $n = 5$ biological replicates. Two-way ANOVA test was used to evaluate significance. The *P* values and number of mice used in each group are indicated in the plots and/or in Source Data.

Online content

Any methods, additional references, Nature Research reporting summaries, source data, statements of code and data availability and associated accession codes are available at https://doi.org/10.1038/s41587-019-0246-4.

Received: 28 November 2018; Accepted: 1 August 2019;
Published online: 23 September 2019

References

1. Chen, D. S. & Mellman, I. Oncology meets immunology: the cancer-immunity cycle. *Immunity* **39**, 1–10 (2013).
2. Tumeh, P. C. et al. PD-1 blockade induces responses by inhibiting adaptive immune resistance. *Nature* **515**, 568 (2014).
3. Kvistborg, P. et al. Anti-CTLA-4 therapy broadens the melanoma-reactive CD8(+) T cell response. *Sci. Transl. Med.* **6**, 254ra128 (2014).
4. Ribas, A. Tumor immunotherapy directed at PD-1. *New Engl. J. Med.* **366**, 2517–2519 (2012).
5. Pardoll, D. M. The blockade of immune checkpoints in cancer immunotherapy. *Nat. Rev. Cancer* **12**, 252–264 (2012).
6. Omuro, A. et al. Nivolumab with or without ipilimumab in patients with recurrent glioblastoma: results from exploratory phase I cohorts of CheckMate 143. *Neuro Oncol.* **20**, 674–686 (2018).
7. O'Rourke, D. M. et al. A single dose of peripherally infused EGFRvIII-directed CAR T cells mediates antigen loss and induces adaptive resistance in patients with recurrent glioblastoma. *Sci. Transl. Med.* **9**, eaaa0984 (2017).
8. Chow, R. D. et al. AAV-mediated direct in vivo CRISPR screen identifies functional suppressors in glioblastoma. *Nat. Neurosci.* **20**, 1329–1341 (2017).
9. Wang, G. et al. Mapping a functional cancer genome atlas of tumor suppressors in mouse liver using AAV-CRISPR-mediated direct in vivo screening. *Sci. Adv.* **4**, eaao5508 (2018).
10. Mates, L. et al. Molecular evolution of a novel hyperactive Sleeping Beauty transposase enables robust stable gene transfer in vertebrates. *Nat. Genet.* **41**, 753–761 (2009).
11. Colella, P., Ronzitti, G. & Mingozzi, F. Emerging issues in AAV-mediated in vivo gene therapy. *Mol. Ther. Methods Clin. Dev.* **8**, 87–104 (2018).
12. Wang, D., Tai, P. W. L. & Gao, G. P. Adeno-associated virus vector as a platform for gene therapy delivery. *Nat. Rev. Drug Discov.* **18**, 358–378 (2019).
13. Platt, R. J. et al. CRISPR–Cas9 knockin mice for genome editing and cancer modeling. *Cell* **159**, 440–455 (2014).
14. Hogquist, K. A. et al. T-cell receptor antagonist peptides induce positive selection. *Cell* **76**, 17–27 (1994).
15. Workman, C. J., Dugger, K. J. & Vignali, D. A. Cutting edge: molecular analysis of the negative regulatory function of lymphocyte activation gene-3. *J. Immunol.* **169**, 5392–5395 (2002).
16. Workman, C. J. et al. Lymphocyte activation gene-3 (CD223) regulates the size of the expanding T cell population following antigen activation in vivo. *J. Immunol.* **172**, 5450–5455 (2004).

17. Anderson, A. C., Joller, N. & Kuchroo, V. K. Lag-3, Tim-3, and TIGIT: co-inhibitory receptors with specialized functions in immune regulation. *Immunity* **44**, 989–1004 (2016).
18. Huang, C. T. et al. Role of LAG-3 in regulatory T cells. *Immunity* **21**, 503–513 (2004).
19. Smith, L. K. et al. Interleukin-10 directly inhibits CD8(+) T cell function by enhancing N-glycan branching to decrease antigen sensitivity. *Immunity* **48**, 299–312 e295 (2018).
20. Shibui, A. et al. Alteration of immune responses by N-acetylglucosaminyltransferase V during allergic airway inflammation. *Allergol. Int.* **60**, 345–354 (2011).
21. Morgan, R. et al. N-acetylglucosaminyltransferase V (Mgat5)-mediated N-glycosylation negatively regulates Th1 cytokine production by T cells. *J. Immunol.* **173**, 7200–7208 (2004).
22. Sugiura, K. & Stock, C. C. Studies in a tumor spectrum. II. The effect of 2,4,6-triethylenimino-s-triazine on the growth of a variety of mouse and rat tumors. *Cancer* **5**, 979–991 (1952).
23. Louveau, A. et al. Structural and functional features of central nervous system lymphatic vessels. *Nature* **523**, 337–341 (2015).
24. Schlager, C. et al. Effector T-cell trafficking between the leptomeninges and the cerebrospinal fluid. *Nature* **530**, 349 (2016).
25. Khalil, D. N., Smith, E. L., Brentjens, R. J. & Wolchok, J. D. The future of cancer treatment: immunomodulation, CARs and combination immunotherapy. *Nat. Rev. Clin. Oncol.* **13**, 273–290 (2016).
26. Ribas, A. et al. Pembrolizumab versus investigator-choice chemotherapy for ipilimumab-refractory melanoma (KEYNOTE-002): a randomised, controlled, phase 2 trial. *Lancet Oncol.* **16**, 908–918 (2015).
27. Preusser, M., Lim, M., Hafler, D. A., Reardon, D. A. & Sampson, J. H. Prospects of immune checkpoint modulators in the treatment of glioblastoma. *Nat. Rev. Neurol.* **11**, 504–514 (2015).
28. Cloughesy, T. F. et al. Neoadjuvant anti-PD-1 immunotherapy promotes a survival benefit with intratumoral and systemic immune responses in recurrent glioblastoma. *Nat. Med.* **25**, 477–486 (2019).
29. Li, B. et al. Comprehensive analyses of tumor immunity: implications for cancer immunotherapy. *Genome Biol.* **17**, 174 (2016).
30. Reardona, D. A. et al. Randomized phase 3 study evaluating the efficacy and safety of nivolumab vs bevacizumab in patients with recurrent glioblastoma: Checkmate 143. *Neuro Oncol.* **19**, 21–21 (2017).
31. Agarwalla, P., Barnard, Z., Fecci, P., Dranoff, G. & Curry, W. T. Sequential immunotherapy by vaccination with GM-CSF-expressing glioma cells and CTLA-4 blockade effectively treats established murine intracranial tumors. *J. Immunother.* **35**, 385–389 (2012).
32. Fecci, P. E. et al. Systemic CTLA-4 blockade ameliorates glioma-induced changes to the CD4(+) T cell compartment without affecting regulatory T-cell function. *Clin. Cancer Res.* **13**, 2158–2167 (2007).
33. Mathios, D. et al. Anti-PD-1 antitumor immunity is enhanced by local and abrogated by systemic chemotherapy in GBM. *Sci. Transl. Med.* **8**, 370ra180 (2016).
34. Saha, D., Martuza, R. L. & Rabkin, S. D. Macrophage polarization contributes to glioblastoma eradication by combination immunovirotherapy and immune checkpoint blockade. *Cancer Cell* **32**, 253–267.e5 (2017).
35. Kim, J. E. et al. Combination therapy with anti-PD-1, anti-TIM-3, and focal radiation results in regression of murine gliomas. *Clin. Cancer Res.* **23**, 124–136 (2017).
36. Dai, H., Wang, Y., Lu, X. & Han, W. Chimeric antigen receptors modified T-cells for cancer therapy. *J. Natl Cancer Inst.* **108**, djv439 (2016).
37. Brown, C. E. et al. Regression of glioblastoma after chimeric antigen receptor T-cell therapy. *N. Engl. J. Med.* **375**, 2561–2569 (2016).
38. Pellegatta, S. et al. Constitutive and TNFα-inducible expression of chondroitin sulfate proteoglycan 4 in glioblastoma and neurospheres: implications for CAR-T cell therapy. *Sci. Transl. Med.* **10**, eaao2731 (2018).
39. Mount, C. W. et al. Potent antitumor efficacy of anti-GD2 CAR T cells in H3-K27M(+) diffuse midline gliomas. *Nat. Med.* **24**, 572–579 (2018).
40. Bernards, R. Finding effective cancer therapies through loss of function genetic screens. *Curr. Opin. Genet. Dev.* **24**, 23–29 (2014).
41. Okada, M. et al. Blockage of core fucosylation reduces cell-surface expression of PD-1 and promotes anti-tumor immune responses of T cells. *Cell Rep.* **20**, 1017–1028 (2017).
42. Shifrut, E. et al. Genome-wide CRISPR screens in primary human T cells reveal key regulators of immune function. *Cell* **175**, 1958–1971.e15 (2018).
43. Ting, P. Y. et al. Guide Swap enables genome-scale pooled CRISPR–Cas9 screening in human primary cells. *Nat. Methods* **15**, 941–946 (2018).
44. Zhou, P. et al. In vivo discovery of immunotherapy targets in the tumour microenvironment. *Nature* **506**, 52–57 (2014).
45. Chen, R. et al. In vivo RNA interference screens identify regulators of antiviral CD4(+) and CD8(+) T cell differentiation. *Immunity* **41**, 325–338 (2014).
46. Shalem, O. et al. Genome-scale CRISPR–Cas9 knockout screening in human cells. *Science* **343**, 84–87 (2014).
47. Demetriou, M., Granovsky, M., Quaggin, S. & Dennis, J. W. Negative regulation of T-cell activation and autoimmunity by Mgat5 N-glycosylation. *Nature* **409**, 733–739 (2001).
48. Granovsky, M. et al. Suppression of tumor growth and metastasis in Mgat5-deficient mice. *Nat. Med.* **6**, 306–312 (2000).

Acknowledgements

We thank C. Fuchs, D. Hafler, R. Montgomery, D. Rimm and M. Gunel for discussions. We thank S. Lam, L. Shen, Z. Bai, H. Ye, R. Kim and other members of the Chen laboratory, as well as various colleagues in the Department of Genetics, Systems Biology Institute, Cancer Systems Biology Center, MCGD Program, Immunobiology Program, BBS Program, Cancer Center and Stem Cell Center at Yale for assistance and/or discussion. We thank the Center for Genome Analysis, the Center for Molecular Discovery, Pathology Tissue Services, Histology Services, the High Performance Computing Center, West Campus Analytical Chemistry Core and West Campus Imaging Core, the Mass Cytometry Core and Keck Biotechnology Resource Laboratory at Yale for technical support. S.C. is supported by Yale SBI/Genetics Startup Fund, the NIH/NCI (grant nos. DP2CA238295, R01CA231112, U54CA209992-8697, R33CA225498, RF1048811, P50CA196530-A10805, P50CA121974-A08306), the Damon Runyon Dale Frey Award (grant no. DFS-13-15), the Melanoma Research Alliance (grant nos. 412806, 16-003524), St-Baldrick's Foundation (grant no. 426685), the Breast Cancer Alliance, the Cancer Research Institute (CLIP), AACR (grant nos. 499395, 17-20-01-CHEN), The Mary Kay Foundation (grant no. 017-81), The V Foundation (grant no. V2017-022), the Ludwig Family Foundation, DoD (grant no. W81XWH-17-1-0235), the Sontag Foundation and the Chenevert Family Foundation. G.W. is supported by CRI Irvington and RJ Anderson Fellowships. X.D. is supported by a Revson Fellowship. M.B.D., R.D.C. and J.J.P. are supported by the Yale MSTP training grant from the NIH (grant no. T32GM007205).

Author contributions

L.Y. designed the AAV–SB–CRISPR vector, developed the screening system and performed the majority of experiments in this study. J.J.P. analyzed the CRISPR screen and other high-throughput data. M.B.D. generated transgenic mice and optimized the screen. R.D.C. designed the Surf library. Q.Y., L.P., Y.D., J.G., G.W. and Y.E. assisted with various experiments. Y.D. and X.D. designed and generated the EGFRvIII CAR-T system. S.C. conceived the study, secured funding and supervised the work. L.Y., J.J.P. and S.C. prepared the manuscript with input from all of the other authors.

Competing interests

A patent application has been filed related to the data in this manuscript.

Additional information

Supplementary information is available for this paper at https://doi.org/10.1038/s41587-019-0246-4.

Correspondence and requests for materials should be addressed to S.C.

Reprints and permissions information is available at www.nature.com/reprints.

Publisher's note Springer Nature remains neutral with regard to jurisdictional claims in published maps and institutional affiliations.

Methods

Institutional approval. This study has received institutional regulatory approval. All recombinant DNA work was performed under the guidelines of the Yale Environment, Health and Safety Committee with an approved protocol (Chen-rDNA-15-45). All animal work was performed under the guidelines of Yale University Institutional Animal Care and Use Committee with approved protocols (Chen-2015-20068 and Chen-2018-20068). All human sample work was performed under the guidelines of Yale University Institutional Review Board with an approved protocol (HIC no. 2000020784). This study uses existing de-identified human samples and data under NIH Exemption 4.

Mice. Rosa26-Cas9-2A-EGFP constitutive expressed mice (*Cas9β* mice), OT-I TCR transgenic mice[14], *Rag1*$^{-/-}$ mice and *C57BL/6J* mice were used in this study. *OT-I;Cas9β* mice were generated by breeding *OT-I* and *Cas9β* mice. *OT-I;Cas9β* and *Cas9β* mice, both female and male, aged 8–12 weeks were used for naïve CD8$^+$ T-cell isolation. For the lateral ventricle injection, 8-week-old female *C57BL/6J* or 7–9-week-old *Rag1*$^{-/-}$ mice were used. Mice were randomly classified into different groups.

Design and synthesis of membrane-bound protein CRISPR knockout library. The gene ontology term GO0009986 was chosen to focus on a set of genes associated with the term 'cell surface'. A total of 1,657 membrane-bound protein-coding genes were selected. Four sgRNAs were chosen per gene similar to the mBrie library design[49], giving a total of 6,628 sgRNAs. A total of 1,000 NTCs were spiked into the library, making the Surf library a total of 7,628 sgRNAs in size (Supplementary Table 1). This membrane-bound protein gene-targeting single-strand RNA (sgRNA) library was named Surf. The membrane-bound protein library was synthesized by massively parallel oligo array synthesis and pooled (CustomArray).

Generation of AAV–CRISPR vector and AAV–Surf library for primary T-cell editing and screening. A hybrid AAV–SB–CRISPR vector for targeting primary mouse T cells (AAV–SB100x) was constructed by gBlock fragments (IDT) followed by Gibson assembly (NEB). The synthesized library was first PCR amplified, then sgRNAs were cloned into double *Bbs* I sites of AAV–CRISPR vector by the Gibson assembly (NEB). The Gibson assembly products were transformed into high-efficiency competent cells (Endura) by electroporation. An estimated library coverage of ≥60× was observed after electroporation. The cloned library was PCR amplified using barcoded primers to ensure proper representation. The cloned library was named AAV–Surf.

AAV production. AAV–SB100x plasmid cloned with library or single sgRNA was packaged similarly to our previously described approach[8]. Details are in the Supplementary Methods.

Cell culture for cell lines and primary T cells. HEK293FT, U87, GL261 and E0771 cell lines were cultured in D10 medium. Mouse naïve CD8$^+$ T cells were cultured in RPMI-1640 (Gibco) medium supplemented with 10% fetal bovine serum, 2 mM L-glutamine, 200 U ml^{-1} penicillin-streptomycin (Gibco) and 49 μM β-mercaptoethanol (Sigma). Details are in the Supplementary Methods.

Generation of stable cell lines. Stable cell lines GL261-FLuc-mCh-cOVA, U87-GFP-Luc-EGFRvIII (U87-GLEvIII) and U87-GFP-Luc (U87-GL) were generated by a combination of procedures including viral transduction, antibiotics selection, FACS sorting and/or single-cell cloning. Flow cytometry was performed again after stable cell lines were established to ensure purity. Details are in the Supplementary Methods.

Splinkerette PCR. *Sleeping Beauty* transposon integration was detected by splinkerette PCR (ref. [50]). Splink 1 and SB-Right1 primers (Supplementary Table 10) were used for the first round of PCR; Splink 2 and SB-Right 2 primers (Supplementary Table 10) were used for the second round of PCR. PCR products were prepared using a Nextera kit (Illumina) and sequenced, then analyzed by custom codes. Details are in the Supplementary Methods.

GBM induction by intracranial surgery and cancer cell transplantation. Same-sex mice were used in each batch of experiments. Mice were anesthetized by intraperitoneal injection of ketamine (100 mg kg^{-1}) and xylazine (10 mg kg^{-1}). They were also administered carprofen (5 mg kg^{-1}) intraperitoneally as a pre-emptive analgesic. Once mice were in deep anesthesia, they were immobilized in a stereotaxic apparatus (Kopf or Stoelting) using intra-aural positioning studs and a tooth bar to immobilize the skull, similar to a previous method[8]. The lateral ventricle was targeted according to the mouse brain stereotaxic coordinates, at approximately 0.6–1.0 mm caudal/posterior to bregma, 0.8–1.5 mm right-side lateral to bregma and 2.0–3.0 mm deep from the pial surface for injection (coordinates: anterior/posterior −0.6 to −1.0, medial/laterial 0.8 to 1.5, dorsal/ventral −2.0 to −3.0). A ~1 mm hole was drilled on the skull surface, via which 1×10^5 to 1.2×10^6 cancer cells were injected into the lateral ventricle with a volume of 4–8 μl, dependent on specific experiments. The injection rate was controlled at 2 μl min^{-1} by an UltraMicroPump 3 (World Precision Instruments). After injection, the incision was closed with tissue adhesive (3M Vetbond) and subcutaneously injected 500 μl lactated Ringer's solution. Mice were placed under the heat lamp until they recovered. Of note, in certain cases, injection of cells into the lateral ventricle may cause leptomeningeal growth instead of GBM. In this study, all GBMs that grew from these experiments that were examined by histology represented a single tumor in each mouse that expanded on the site of injection in a relatively even manner, which also pathologically resembles malignant glioma.

AAV–Surf CD8$^+$ T-cell screen in a syngeneic mouse model of GBM. Naïve CD8$^+$ T cells were isolated from the spleen and lymph modes of Cas9$^+$ mice. A total of 2×10^7 naïve OT-I;Cas9β or Cas9β CD8$^+$ T cells were transduced with 10^{11} AAV–Surf virus particles. Syngeneic mouse models of GBM were set-up with intracranial injection of native or luciferase-expressing GL261 cells (GL261 and GL261-Luc, respectively) transplanted into the lateral ventricle of C57BL/6J mice. AAV–Surf-infected CD8$^+$ T cells were adoptively cell transferred into GBM-engrafted mice via i.v. (tail vein) injection. Three screens were performed. The one with native GL261 GBM (injected with OT-I;Cas9β T cells) reached endpoint sooner (all mice euthanized by 20 d post tumor implantation (dpi), 'shorter-term screen'). The one with GL261-Luc GBM (injected with OT-I;Cas9β T cells) reached endpoint later (all mice euthanized by 92 d post tumor implantation, 'longer-term screen'). The third screen with GL261 GBM (injected with Cas9β T cells) reached endpoint with a duration between the first two (all mice euthanized by 26 d post tumor implantation, 'medium term screen'). With transduction at this level, single cells with functional sgRNA expression are estimated at 48%, which gives a functional MOI estimate of 0.65. In the screen, we euthanize the mice at a synchronized time point, or at the endpoint when the body condition score is <2 if the animal does not survive to the synchronized endpoint (per Yale University Institutional Animal Care and Use Committee protocol). We performed three independent screens; 'medium-term' used seven mice, 'short-term' used three mice and 'long-term' used nine mice for library readout. The number of TILs recovered per brain averaged 5×10^4 from AAV–Vector mice and 1.25×10^5 from AAV–Surf mice.

Adoptive cell transfer. Naïve CD8$^+$ T cells were infected with virus after isolation, and cultured for 3–5 d before i.v. injection. For the shorter-term AAV–Surf screen, 1.8×10^6 OT-I;Cas9β CD8$^+$ T cells were injected. For the longer-term screen, 4×10^6 OT-I;Cas9β CD8$^+$ T cells were injected. In the Cas9β CD8$^+$ T-cell screen, 3×10^6 Cas9β CD8$^+$ T cells were i.v. injected after 10 d tumor engraftment. For the validation experiments, OT-I;Cas9β or Cas9β CD8$^+$ T cells were injected, and numbers of cancer cells and T cells injected are shown in the figures and legends. Adoptive transfer was also performed using an intracranial approach in validation experiments. Note that these two methods of T-cell infusion were not performed head-to-head. After T-cell injection, mice were monitored every day. All animals were deemed for euthanasia when they developed macrocephaly, poor body condition or other euthanasia criteria according to the approved animal protocol. Brains were isolated and stored at −80 °C for genomic DNA extraction and readout, or fixed in 4% paraformaldehyde for hematoxylin and eosin staining.

sgRNA readout and deep sequencing. Two rounds of PCR reactions were used for the sgRNA library readout. PCR primers were provided (Supplementary Table 2). Details are in the Supplementary Methods.

AAV–SB–CRISPR screen data processing. Raw single-end fastq read files were filtered and demultiplexed using Cutadapt[51]. To remove extra sequences downstream (that is, the 3′ end) of the sgRNA spacer sequences, the following settings were used: cutadapt --discard-untrimmed -a GTTTTAGAGCTAGAAATGGC. As the forward PCR primers used to readout sgRNA representation were designed to have a variety of barcodes to facilitate multiplexed sequencing, these filtered reads were then demultiplexed with the following settings: cutadapt -g file:fbc.fasta --no-trim, where fbc.fasta contained the 12 possible barcode sequences within the forward primers. Finally, to remove extra sequences upstream (that is, the 5′ end) of the sgRNA spacers, the following settings were used: cutadapt --discard-untrimmed –g GTGGAAAGGACGAAACACCG. Through this procedure, the raw fastq read files could be pared down to the 20 base pair sgRNA spacer sequences. The 20 base pair sgRNA spacer sequences from each demulitplexed sample were then mapped to the designed sgRNA spacers in the surface library (Supplementary Table 1). A bowtie index of the sgRNA library was generated using the bowtie-build command in Bowtie v.1.1.2 (ref. [52]). The filtered fastq read files were mapped to the index using the following settings: bowtie -v 1 --suppress 4,5,6,7 --chunkmbs 2000 –best. Using the resultant mapping output, the number of reads that had mapped to each sgRNA within the library was quantified.

Analysis of CRISPR screens using RIGER. For RIGER analysis of CRISPR screens, read count tables were used to calculate log fold changes for tumor versus cell samples to score and rank sgRNAs, with ties in rank broken by random order. These data were then used as input to a Java-based implementation of RIGER (https://github.com/broadinstitute/rigerj) to generate *P* values and gene rankings based on consistent enrichment across multiple sgRNAs for identification of

candidate genes[46]. Both the second highest-ranking sgRNA and the weighted sum scoring methods were used for computation of gene rankings, and compared to ensure consistency between methods.

T-cell adoptive transfer with subcutaneous tumor models. GL261-FLuc-mCh-rOVA cells and E0771-mCh-rOVA cells were subcutaneously injected into male *Rag1*$^{-/-}$ mice for modeling GBM and TNBC, respectively. Adoptive transfer of T cells was performed similarly to above. Details are in the Supplementary Methods.

Mouse brain tumor studies. Mouse brain tumor monitoring, IVIS imaging, brain dissection and histology were performed using standard tumor study procedures. Details are in the Supplementary Methods.

Flow cytometry. Flow cytometry was performed using standard immunology methods. Details are in the Supplementary Methods.

Standard molecular biology. Experiments such as DNA/RNA preparation, T7 endonuclease I assay (T7EI), RT–qPCR and electrophoresis were performed following standard molecular biology protocols. Primers for T7E1 are provided in Supplementary Table 7. Additional details are in the Supplementary Methods.

Detection of AAV–mediated mutagenesis by Nextera. The PCR products were used for Nextera library preparation following manufacturer protocols (Illumina). Reads were mapped to the amplicon sequences using BWA-MEM (ref. [53]) at default settings. Indel variants were first processed with Samtools[54] with the settings samtools mpileup -d 1000000, then piped into VarScan v.2.4.1 (ref. [55]) with the settings pileup2indel --min-coverage 2 --min-reads2 2 --min-var-freq 0.00001. The indels are provided in Supplementary Datasets 7–9.

Human primary CD8$^+$ T-cell endogenous gene knockout. Human primary CD8$^+$ T cells were isolated from healthy donors, stimulated with anti-CD3/CD28 beads (Invitrogen) and cultured in X-VIVO 15 medium (Lonza) supplied with 5% human serum and IL-2. Gene knockout was performed by Cas9 RNP electroporation. Details are in the Supplementary Methods.

***PDIA3*$^{-/-}$-EGFRvIII-CAR-T-cell establishment.** NTCs (NTC CRISPR RNA (crRNA) electroporated T cells) and *PDIA3*$^{-/-}$ primary CD8$^+$ T cells were targeted with *TRAC* locus RNP complex; a total of ~6×10^9 viral genome copies of AAV6 homology-directed repair donor (LHA-EFS-EGFRvIII-CAR-RHA) were added into each electroporated T-cell reaction (3×10^6 T cells per reaction) within 1 h after electroporation. Oligos used for EGFRvIII CAR-T generation and detection are provided in Supplementary Table 11.

Human *PDIA3*$^{-/-}$-EGFRvIII-CAR-T-cell coculture (kill) assay. To sensitively detect *PDIA3*$^{-/-}$-EGFRvIII-CAR-T-cell killing efficacy, U87-GL and U87-GLEvIII cell lines were established. First, 2×10^4 U87-GL or U87-GLEvIII cells were seeded in a 96-well white polystyrene plate, then different T cell/cancer cell ratio cocultures were set up. Cancer cell killing was measured after 24 h of coculture by adding 150 μg ml^{-1} D-luciferin (PerkinElmer) using a multichannel pipette. Luciferase intensity was measured with a plate reader (PerkinElmer).

Mass cytometry (CyTOF). Targeting efficiency of *PDIA3* was confirmed by surveyor assay and Nextera sequencing. Human CD8$^+$ T cells were collected and washed with PBS; then, cells were resuspended to 1×10^7 ml^{-1} in PBS and Cell-ID Cisplatin (Fluidigm) was added to a final concentration of 5 μM. Cells were incubated at room temperature for 5 min, then washed with Maxpar Cell Staining Buffer (Fluidigm). Each replicate was aliquoted with 2×10^6 cells in a volume of 50 μl, and 50 μl staining buffer with surface marker antibody cocktail (Supplementary Table 8) (Fluidigm or provided by the Yale CyTOF core) was added to each tube. The tube was gently mixed with a pipette and incubated at room temperature for 30 min. Following the incubation, cells were washed with Maxpar Cell Staining Buffer twice. Cells were fixed by adding 500 μl Maxpar Fix I Buffer (Fluidigm) to each tube, and incubated for 15 min at room temperature. Cells were then washed with Maxpar Perm-S Buffer (Fluidigm) twice. Next, 50 μl staining buffer with cytoplasmic/secreted antibody cocktail (Supplementary Table 8) was added into fixed cells which were resuspended in 50 μl Maxpar Cell Staining Buffer. Cells were incubated at room temperature for 30 min. After incubation, cells were washed with Maxpar Cell Staining Buffer twice. Finally, cells were incubated in intercalation solution (Fluidigm) at a final concentration of 125 nM, then incubated overnight at 4 °C. Before running on a CyTOF machine, cells were washed with Maxpar Cell Staining Buffer and cell concentration was adjusted to 5–7×10^5 per ml with water. All data were collected on a CyTOF Helios instrument (Fluidigm).

CyTOF data processing. CyTOF quality control prefiltering was performed by gating in FlowJo (live-dead, CD3, CD8). Channel signal values were exported as CSV and analyzed using custom scripts in R. Dimensionality reduction was performed by *t*-distributed stochastic neighbor embedding (t-SNE) (Rtsne package), followed by *k*-means and hierarchical clustering.

Immunoblot and TCR signaling. Immunoblots were performed with standard molecular biology methods. TCR signaling was performed using standard western blot with phospho-specific antibodies. Details are in the Supplementary Methods.

scRNA-seq. Naïve CD8$^+$ T cells were isolated from OT-I;Cas9 mice; T cells were stimulated with anti-CD3ε and anti-CD28 as previously described. CD8$^+$ T cells were infected with AAV6-sgPdia3 and AAV6-Vector after being activated. At day 5 after AAV infection, T cells were collected and dead cells were removed using Dead Cell Removal Kit (Miltenyi Biotec). T cells were resuspended in PBS to a concentration of 1×10^6 per ml. Ten thousand CD8$^+$ T cells per sample were used for scRNA-seq by following the protocol provided by 10x Genomics. Data processing details are in the Supplementary Methods.

scRNA-seq data processing. Read count matrices from scRNA-seq samples were obtained by mapping using native 10x Cell Ranger output. Samples were pooled together into a single CSV and analyzed using custom scripts in R. Reads were prefiltered by ribosomal and mitochondrial genes, normalized by cells per 10,000 reads, then log transformed. For cell percentage quantifications, cells were first prefiltered, in order, by Ptprc$^+$, Cd3e$^+$, Cd8a$^+$ and Cd4$^-$ expression. Marker expression status on high-confidence Cd8 cells was then quantified individually for each marker of interest. Expression status for a given gene was thresholded at 0.1 normalized read value. Differential expression between sgPdia3 and AAV–Vector control was performed by two-sided Wilcoxon signed-rank test by gene, with *P* values adjusted by the Benjamini and Hochberg method. Significance was compared with differences in mean expression between populations. Dimensionality reduction was performed by t-SNE (Rtsne package), followed by *k*-means and hierarchical clustering. Heatmap.2 function was used to show normalized gene expression for most variable genes.

Bulk mRNA-seq. Activated OT-I;Cas9β CD8$^+$ T cells were transduced with AAV–sgPdia3 or AAV–Vector virus. At day 4 after transduction, a small portion of T cells was collected for surveyor assay to ensure *Pdia3* knockout before performing the RNA-seq library preparations. mRNA library preparation was performed at day 5 after virus transduction using a NEBNext Ultra RNA Library Prep Kit for Illumina. Samples were multiplexed using barcoded primers provided by NEBNext Multiplex Oligos for Illumina (Index Primers Set 1). Libraries were sequenced with HiSeq 4000 or Novaseq systems (Illumina).

Metadata for mRNA-seq can be found in Supplementary Table 9.

mRNA-seq data processing. Raw FASTQ files from mRNA-seq were analyzed for transcript quantification using the Kalliso quant algorithm[56] with the setting -b 100, and differential gene expression was performed with Sleuth[57]. Transcriptome references were obtained from Ensembl. Differentially upregulated and downregulated genes with cutoff of *Q* value 1×10^{-3} were used for DAVID analysis[58], and genes belonging to select enriched gene ontology terms were used for generating heatmaps. Z-scores for heatmaps were calculated on $\log_2$-normalized gene counts scaled by genes. Visualizations of differentially expressed genes, including volcano plot and heatmaps, were performed using standard R packages including ggplot2 and VennDiagram.

Large-scale patient T-cell immune signature data analysis using TIDE. The gene signatures of T-cell dysfunction and prediction of cancer immunotherapy response on cancer patient data were performed using the TIDE algorithm as previously described[59]. Gene expression level of PDIA3 was associated with CTL-mediated patient survival with or without checkpoint blockade treatment.

Standard statistical analysis. All statistical methods are described in figure legends and/or supplementary Excel tables. The *P* values and statistical significance were estimated for all analyses. Prism (GraphPad Software) and RStudio were used for these analyses. Additional information can be found in the Nature Research Reporting Summary.

Reporting Summary. Further information on research design is available in the Nature Research Reporting Summary linked to this article.

Data availability

Source data and statistics for non-NGS experiments such as tumor studies, flow cytometry, T7E1, qPCR, protein experiments and coculture assays are provided in an Excel table as Source Data. Genome sequencing data are deposited to the Sequence Read Archive with accession number PRJNA553676. Other data, reagents, methods, computational code and materials that support the findings of this research are available from the corresponding author upon reasonable request.

Code availability

Custom code used to support the findings of this research is available from the corresponding author upon reasonable request.

References

49. Doench, J. G. et al. Rational design of highly active sgRNAs for CRISPR–Cas9-mediated gene inactivation. *Nat. Biotechnol.* **32**, 1262–1267 (2014).
50. Uren, A. G. et al. A high-throughput splinkerette-PCR method for the isolation and sequencing of retroviral insertion sites. *Nat. Protoc.* **4**, 789–798 (2009).
51. Martin, M. Cutadapt removes adapter sequences from high-throughput sequencing reads. *EMBnet.journal* **17**, 10–12 (2011).
52. Langmead, B., Trapnell, C., Pop, M. & Salzberg, S. L. Ultrafast and memory-efficient alignment of short DNA sequences to the human genome. *Genome Biol.* **10**, R25 (2009).
53. Li, H. & Durbin, R. Fast and accurate short read alignment with Burrows–Wheeler transform. *Bioinformatics* **25**, 1754–1760 (2009).
54. Li, H. et al. The Sequence Alignment/Map format and SAMtools. *Bioinformatics* **25**, 2078–2079 (2009).
55. Koboldt, D. C. et al. VarScan: variant detection in massively parallel sequencing of individual and pooled samples. *Bioinformatics* **25**, 2283–2285 (2009).
56. Bray, N. L., Pimentel, H., Melsted, P. & Pachter, L. Near-optimal probabilistic RNA-seq quantification. *Nat. Biotechnol.* **34**, 525–527 (2016).
57. Pimentel, H., Bray, N. L., Puente, S., Melsted, P. & Pachter, L. Differential analysis of RNA-seq incorporating quantification uncertainty. *Nat. Methods* **14**, 687–690 (2017).
58. Huang da, W., Sherman, B. T. & Lempicki, R. A. Systematic and integrative analysis of large gene lists using DAVID bioinformatics resources. *Nat. Protoc.* **4**, 44–57 (2009).
59. Jiang, P. et al. Signatures of T cell dysfunction and exclusion predict cancer immunotherapy response. *Nat. Med.* **24**, 1550–1558 (2018).

nature research

Corresponding author(s): Sidi Chen

Last updated by author(s): Jul 14, 2019

Reporting Summary

Nature Research wishes to improve the reproducibility of the work that we publish. This form provides structure for consistency and transparency in reporting. For further information on Nature Research policies, see Authors & Referees and the Editorial Policy Checklist.

Statistics

For all statistical analyses, confirm that the following items are present in the figure legend, table legend, main text, or Methods section.

n/a	Confirmed	
☐	☒	The exact sample size (*n*) for each experimental group/condition, given as a discrete number and unit of measurement
☐	☒	A statement on whether measurements were taken from distinct samples or whether the same sample was measured repeatedly
☐	☒	The statistical test(s) used AND whether they are one- or two-sided *Only common tests should be described solely by name; describe more complex techniques in the Methods section.*
☐	☒	A description of all covariates tested
☐	☒	A description of any assumptions or corrections, such as tests of normality and adjustment for multiple comparisons
☐	☒	A full description of the statistical parameters including central tendency (e.g. means) or other basic estimates (e.g. regression coefficient) AND variation (e.g. standard deviation) or associated estimates of uncertainty (e.g. confidence intervals)
☐	☒	For null hypothesis testing, the test statistic (e.g. *F*, *t*, *r*) with confidence intervals, effect sizes, degrees of freedom and *P* value noted *Give P values as exact values whenever suitable.*
☒	☐	For Bayesian analysis, information on the choice of priors and Markov chain Monte Carlo settings
☐	☒	For hierarchical and complex designs, identification of the appropriate level for tests and full reporting of outcomes
☐	☒	Estimates of effect sizes (e.g. Cohen's *d*, Pearson's *r*), indicating how they were calculated

Our web collection on statistics for biologists contains articles on many of the points above.

Software and code

Policy information about availability of computer code

Data collection	Flow cytometric data were collected using BD FACSDiva software version 6.0.
Data analysis	FlowJo for FACS, Fiji for Western blot, DNAstar for DNA, Prism for small scale data analysis. Custom codes were used for analyzing high-throughput datasets. Codes that support the findings of this research are available from the corresponding author upon reasonable request.

For manuscripts utilizing custom algorithms or software that are central to the research but not yet described in published literature, software must be made available to editors/reviewers. We strongly encourage code deposition in a community repository (e.g. GitHub). See the Nature Research guidelines for submitting code & software for further information.

Data

Policy information about availability of data

All manuscripts must include a data availability statement. This statement should provide the following information, where applicable:

- Accession codes, unique identifiers, or web links for publicly available datasets
- A list of figures that have associated raw data
- A description of any restrictions on data availability

Source data and statistics for non-NGS experiments such as tumor studies, flow cytometry, T7E1, qPCR, protein experiments, and co-culture assays are provided in an excel table as a supplemental material. Genome sequencing data are deposited to SRA with an accession number: PRJNA553676. Other data, reagents, methods, computational codes and materials that support the findings of this research are available from the corresponding author upon reasonable request.

Field-specific reporting

Please select the one below that is the best fit for your research. If you are not sure, read the appropriate sections before making your selection.

☒ Life sciences ☐ Behavioural & social sciences ☐ Ecological, evolutionary & environmental sciences

For a reference copy of the document with all sections, see nature.com/documents/nr-reporting-summary-flat.pdf

Life sciences study design

All studies must disclose on these points even when the disclosure is negative.

Sample size	For most cases, biological triplicate experiments were performed unless otherwise noted. Details on sample size for experiments were indicated in methods and figure legends. No statistical methods were used to predetermine the sample size. Sample sizes for experiments were estimated based on previous experience with similar setups that showed significance.
Data exclusions	No data was excluded in this study.
Replication	Experiments were performed with replication and the findings were successful reproduced.
Randomization	Samples were randomized into experimental or control groups. Animals were randomized into different treatment groups.
Blinding	The investigators were blinded during tumor size measurement, screen data processing using barcoded metadata, but were not blinded for other data collection or analysis, which did not affect reproducibility.

Reporting for specific materials, systems and methods

We require information from authors about some types of materials, experimental systems and methods used in many studies. Here, indicate whether each material, system or method listed is relevant to your study. If you are not sure if a list item applies to your research, read the appropriate section before selecting a response.

Materials & experimental systems

n/a	Involved in the study
☐	☒ Antibodies
☐	☒ Eukaryotic cell lines
☒	☐ Palaeontology
☐	☒ Animals and other organisms
☒	☐ Human research participants
☐	☒ Clinical data

Methods

n/a	Involved in the study
☒	☐ ChIP-seq
☐	☒ Flow cytometry
☒	☐ MRI-based neuroimaging

Antibodies

Antibodies used

anti-CD3 APC (Mouse, Biolegend, Clone:17A2, Cat:100236), anti-CD3 PE/Cy7 (Mouse, Biolegend, Clone:17A2, Cat:100220), anti-CD3ε (Mouse, Biolegend, Clone: 145-2C11, Cat:100340), anti-CD28 (Mouse, Biolegend, Clone: 37.51, Cat:102116), anti-CD8 APC (Mouse, Biolegend, Clone:53-6.7, Cat:100712), anti-CD8 FITC (Mouse, Biolegend, Clone: 53-6.7, Cat: 100706), anti-CD8 PE/Cy7 (Mouse, Biolegend, Clone: 53-6.7, Cat: 100722), anti-IFNg APC (Mouse, Biolegend, Clone: XMG1.2, Cat:505810), anti-CD45.2 APC (Mouse, Biolegend, Clone: 104, Cat:109814), anti-CD45.1 FITC (Mouse, Biolegend, Clone: A20, Cat: 110706), anti-PD1 PE (Mouse, Biolegend, Clone: 29F.1A12, Cat: 135206), anti-Lag3 PE (Mouse, Biolegend, Clone: 11C3C65, Cat: 369306), anti-Tim3 PE (Mouse, Biolegend, Clone: B8.2C12, Cat: 134004), anti-CD3 FITC (Human, Biolegend, Clone: HIT3a, Cat: 300306), anti-CD8 APC/Cy7 (Human, Biolegend, Clone: HIT8a, Cat: 300926), anti-IFNg APC (Human, Biolegend, Clone: 4S.B3, Cat:502512), anti-CD28 (human, Biolegend, Clone: CD28.2, Cat:302934).

All CyTOF antibodies were for human experiments and purchased from Fluidigm or Yale CyTOF core. CD45RA (Clone: HI100, Cat: 3143006B), CD8a (Clone: RPAT8, Cat: 3146001B), CD45RO (Clone: UCHL1, Cat: 3164007B), CD3 (Clone: UCHT1, Cat: 3170001B), CD45 (Clone: HI30, Cat: 3089003B), CD95/Fas (Clone: DX2, Cat: 3152017B), CXCR3 (Clone: G025H7, Cat: 3163004B), CD127 (Clone: A019D5), CD62L (Clone: DREG-56, Cat: V00751), IL-2 (Clone: MQ117H12, Cat: 3158007B), IL-10 (Clone: JES3-19F1, Cat: V06009), CD134 (Clone: ACT35, Cat: 3150023B), TIM3 (Clone: F382E2, Cat: 3153008B), PD1 (Clone: EH12.2H7, Cat: 3155009B), CTLA4 (Clone: 14D3, Cat: 3161004B), CD278 (Clone: C398.4A, Cat: 3168024B), CD137 (Clone: 4B4-1, Cat: 3173015B), LAG3 (Clone: 11C3C65, Cat: 3175033B).

Anti-human PDIA3 (HPA003230, Atlas).Anti-Plcγ1 (Cat: 2822, CST), anti-phospho-Plcγ1 (Cat: 2821, CST), anti-Erk1/2 (Cat: 9102, CST), anti-phospho-ERK1/2 (Cat: 9101, CST), Anti-vinculin (ab129002, Abcam), anti-GAPDH (ab9485, Abcam).

Validation

All antibodies were validated by staining positive cell lines using protocols provided from manufactory before doing formal experiments.

Eukaryotic cell lines

Policy information about cell lines

Cell line source(s)	HEK239FT and GL261 were sourced from ATCC, U87 was from NCI/Charles River, E0771 form C3H, human CD8 T cells from Stem Cell.
Authentication	All cell lines used have been authenticated by the original vendors. Cell lines from ATCC have been thoroughly tested and authenticated, using morphology, karyotyping, and PCR based approaches to confirm the identity of cell lines and to rule out both intra- and interspecies contamination.

Mycoplasma contamination	All cell lines tested negative for mycoplasma contamination.
Commonly misidentified lines (See ICLAC register)	No misidenified cell lines were used in the study.

Animals and other organisms

Policy information about studies involving animals; ARRIVE guidelines recommended for reporting animal research

Laboratory animals	Both female and male, aged 8-12 weeks of Cas9beta (Rosa26-Cas9),OT-I;Cas9beta, CD45.1 and CD45.2 mice were used. 8 week-old female C57BL/6J and 7-9 week-old female Rag1-/- mice were used for brain injection.
Wild animals	The study did not involve in wild animals.
Field-collected samples	The study did not involve samples collected from the field.
Ethics oversight	All animal work was performed with Yale IACUC approved protocols (Chen-2015-20068 and Chen-2018-20068).

Note that full information on the approval of the study protocol must also be provided in the manuscript.

Clinical data

Policy information about clinical studies

All manuscripts should comply with the ICMJE guidelines for publication of clinical research and a completed CONSORT checklist must be included with all submissions.

Clinical trial registration	N/A
Study protocol	HIC#2000020784
Data collection	Analysis of previously collected de-identified clinical data using TIDE (http://tide.dfci.harvard.edu/). Analysis of previously collected de-identified human PBMCs / T cells using flow or CyTOF (Exemption 4).
Outcomes	Survival outcome were analyzed for de-identified clinical data using TIDE. No new outcome data were generated.

Flow Cytometry

Plots

Confirm that:

☒ The axis labels state the marker and fluorochrome used (e.g. CD4-FITC).

☒ The axis scales are clearly visible. Include numbers along axes only for bottom left plot of group (a 'group' is an analysis of identical markers).

☒ All plots are contour plots with outliers or pseudocolor plots.

☒ A numerical value for number of cells or percentage (with statistics) is provided.

Methodology

Sample preparation	Samples were prepared from mouse spleen and lymph nodes. For analysis of mouse brain CD8 T cells, brain tissue were digested by collagenase, dispase and DNase I.
Instrument	Flow cytometry data were acquired by BD FACSAria cytometer (BD Bioscences)
Software	FlowJo software (Threestar, Ashland, OR) was used for flow cytometry data analysis.
Cell population abundance	When cells were sorted or enriched, the purity was confirmed by flow cytometry and in each case was above 90% purity.
Gating strategy	Cells were first gated by FSC/SSC. To distinguish between positive and negative of each channel, non-stained control samples were analyzed and utilized as background. For the purity analysis of GL261-mCherry-OVA cells, GL261 cells were used as background. For the purity analysis of U87-GL and U87-GL-EGFRvIII cells, U87 cells were used as background.

☒ Tick this box to confirm that a figure exemplifying the gating strategy is provided in the Supplementary Information.